The possible synglaciogenic Ediacaran hematitic banded iron salt formation (BISF) at Hormuz Island, southern Iran: Implications for a new style of exhalative hydrothermal iron-salt system

Habibeh Atapour [a,*], Alijan Aftabi [b]

[a] Department of Mining Engineering, Shahid Bahonar University of Kerman, P.O. Box 76135-133, Kerman, Iran
[b] Department of Geology, Shahid Bahonar University of Kerman, P.O. Box 76135-133, Kerman, Iran

ABSTRACT

The Ediacaran BISF at Hormuz Island is a newly identified glaciogenic iron-salt deposit in the Tethyan margin of Gondwana. The BISF was formed by synchronous riftogenic A-type submarine felsic volcanism and evaporate deposition. The mineralization occurs in a proximal felsic tuff cone and jaspilitic distal zones and contains 1 million tonne of hematite-rich ore with an average grade of 58% Fe. The ore structure shows cyclicity of macrobandings, mesobandings and microbandings of anhydrite, halite, hematite and chert, which marks a new record in BIFs geohistory. The alteration minerals in the proximal and distal zones are actinolite, ripidolite, epidote, sericite, tourmaline, clinochlore, anhydrite and clay minerals. The occurrence of metamorphosed polygenetic bullet-shape dropstones in BISF attests that there was probably a continuous process of ice melting, episodic submarine volcanism and exhalative hydrothermal banded iron salt formation during the Late Ediacaran time. The non-metamorphosed Neoproterozoic stratigraphy, the presence of genus Collenia, U-Pb dating (558 ± 7 Ma) and the marked negative $\delta^{13}C$ excursion in cap carbonates are representative of Late Ediacaran glaciation, which has been identified worldwide. The REE+Y display light REE enrichment, unusually strong Tb-Tm anomaly, a weak positive Y anomaly, but no distinguished Eu and Ce anomalies, reflecting the glaciogenic nature of the BISF. The contents of Zr, Hf, Nb, Ta, Th, La, Ce and Y in BISF, dropstones, halite and cap carbonates are similar to those of the Neoproterozoic glaciogenic BIFs. Also, the Ni/Fe, P/Fe ratios and Fe/Ti – Al/Al + Fe + Mn + Ca + Na + K diagram suggest an exhalative hydrothermal Ediacaran-type BISF. The absence of brecciated magnetite in the ore association and the low contents of copper (9–493 ppm) and gold (<5–8 ppb) are not in favor of the IOCG – Kiruna-type iron oxide ores. The co-paragenesis of hematite with several alteration minerals, in particular actinolite, tourmaline and anhydrite, indicates that the exhalative hydrothermal fluids were generated by the interaction of seawater with the felsic rocks and sediments at about 200– 500 °C. The interaction of seawater with felsic magma and sediments led to the formation of Mg-rich alteration minerals, leaching Si, Fe, Mn and other elements and forming the potential ore fluids. It is highlighted that the A-type alkaline submarine felsic volcanism could be considered as an exploration target for BISF.

1. Introduction

Neoproterozoic glaciomarine BIFs of the Rapitan-type are well-documented (Gaucher et al., 2015; Mohseni and Aftabi, 2015; Hagemann et al., 2016). On the other hand, the geological, structural and petrogeochemical signatures of the dropstone-bearing Ediacaran banded iron salt formations have been attracting increased attention only recently. In fact, there are no recorded data on the co-occurrence of banded jaspilitic hematite and salt formation. Neoproterozoic jaspilite and hematite-rich banded iron formations are reported to be intimately associated with glaciogenic dropstones and siliclastics (Yeo, 1981; Klein and Beukes, 1993; Lottermoser and Ahshley, 2000; Young, 2002, 2013; Holland, 2005; Aftabi et al., 2009; Pecoits et al., 2009; Pirajno, 2009; Cox et al., 2013; Sagiroglu et al., 2013; Mohseni and Aftabi, 2015). This is based on the "Snowball Earth" model (Hoffman et al., 1998; Shields, 2005). The model describes the build-up of ferrous iron in the oceans during glacial periods in the Late Proterozoic, followed by oxidation and deposition of the iron, silica,

diamictites and dropstones during the interglacial periods. According to Yeo (1981) and Young (2002) widespread Late Proterozoic Red Sea type rifting is considered to be the main possible factor for exhalative hydrothermal banded iron formations and related glaciogenic sequences. The mineralogy of the Neoproterozoic banded iron formations is simple and composed of hematite, chert, quartz, chlorite, sericite, biotite, carbonates, plagioclase, apatite and tourmaline with minor magnetite (Klein and Beukes, 1993).

The reappearance of glaciogenic BIFs in the Neoproterozoic (800–542 Ma) has been discussed, although Holland (2005, p. 1500) considered that the reappearance of the BIFs was caused by the deep circulation of ocean water returned from a highly oxidized to a mildly reduced condition. Klein and Beukes (1993) reported that the Neoproterozoic banded iron formations and their associated glaciogenic rocks are widespread in all continents. Concerning this, Fig. 1A illustrates the most recognized Cryogenian and Ediacaran banded iron formations. Neoproterozoic banded iron formations contain high content of phosphorous (1.24 wt%) and formed during Tonian (1000–850 Ma), Cryogenian (850–630 Ma) and Ediacaran 635–542 Ma) periods (Ilyin, 2009). Previous studies on the Hormuz salt dome have only described the geology (Kent, 1979; Hurford et al., 1984), and U-Pb geochronology on zircon (Alavi, 2004; Faramarzi et al., 2015). Valuable stable isotopic data on sulfur, oxygen and carbon were also performed by Houghton (1980) and Ghazban and Al-Aasm (2010).

Descriptions of Iranian banded iron formations are rare, except for the few examples reported by Aftabi (2001), Aftabi et al. (2009), Atapour and Aftabi (2012), Mohseni and Aftabi (2015), and Atapour and Aftabi (2017). Of these, the Ediacaran Fe-P ores of Bafq mining district (E4) and Hormuz Fe-salt ore (E5) are shown on Fig. 1A. The main objectives of this paper are (1) to document new recorded glaciogenic structural and textural relations in BISF (2) interpret the geochemical and isotopic data in rhyolites, ores, diamictites, dropstones and cap carbonates and (3) discuss the possible genetic and exploration model for the Ediacaran BISF.

2. Paleotectonics and geological setting of Hormuz Island

During the Neoproterozoic, the Proto-Iranian microplate was connected to the northeastern margin of the Gondwana supercontinent (Figs. 1B and 2). The Hormuz Complex formed unconformably on the eroded metamorphic basement of the Pan-African orogen and in riftogenic salt basins associated with submarine felsic volcanism (Husseini, 1988; Talbot et al., 2009; Atapour and Aftabi, 2017). In the Late Neoproterozoic or Ediacaran time (635–542 Ma) widespread intra-plate A-type alkaline sub-aerial volcanism occurred during the Pan-African orogen (El-Bialy and Hassen, 2012; Atapour and Aftabi, 2017). Importantly, this phase of magmatism erupted as submarine felsic volcanism and was synchronously associated with salt formation at the Hormuz Island in the Persian Gulf. Similar submarine felsic volcanism and banded iron formation was also reported by Pelleter et al. (2006) in southeastern Morocco.

The circular Hormuz Island with a diameter of 7 km is located in the strait of Hormuz, southeast of Bander Abbas, Hormuzgan province in the Persian Gulf, Iran (Fig. 2). The Island is a part of the Neoproterozoic salt basins of southeastern Persian Gulf in Zagros Folded Belt (Fig. 2). The belt belongs to the Alpine-Himalayan orogenic mountain range (Gansser, 1992; Stocklin, 1968; Ala, 1974; Edgell, 1991). The Hormuz rock salts and associated volcano-sedimentary units, known as Hormuz Complex (Stocklin, 1968) were deposited unconformably on the eroded basements of the Pan-African orogen (1000–640 Ma) in a shallow rifted composite graben basin, trending northwest along the Tethyan margin of Gondwana in Saudi Arabia, Zagros mountains of Iran and Oman

(Kent, 1979; Husseini, 1988; Aftabi, 2001; Talbot et al., 2009). The NE-SW and N-S trends of Pan-African basement faults may have controlled the riftogenic graben basins for synchronous felsic volcanism associated with shallow marine salt deposition in the Persian Gulf and the Arabian Peninsula (Edgell, 1991). The proto-Tethys riftogenic basins formed as aulacogen-type volcano-sedimentary basins, but failed to open into an ocean (Aftabi, 2001; Talbot et al., 2009). Stocklin (1968) suggested a possible rifting belt that trends from Rub Al-Khali in Arabian plate through Hormuz Island. There is a possibility that the continuation of the similar rift zones have formed shallow aulacogen basins for the formation of the Neoproterozoic-Early Paleozoic banded iron formations in the Gole Gohar iron mine, Jalalabad mine, Bafq iron mining district, and iron–base metal mineralization of Taknar area in the Iranian microplate (Fig. 2, number 1–5). The Tethyan margin of Gondwana includes several Neoproterozoic-Early Paleozoic salt plug domes in the Persian Gulf, Oman, Bahrin, Qatar and Saudi Arabia. These salt plug islands are exposed as a result of extrusion and remobilization of the evaporites (Nasir et al., 2008; Talbot et al., 2009). In terms of regional stratigraphy, most of the salt plugs are composed of volcano-sedimentary sequences (e.g., rhyodacitic-rhyolitic tuffs, keratophyric rhyolites, banded hematite, shale, dolomite, sandstone) and their syngenetic evaporites (carbonates, anhydrite, halite, sylvite). Despite the incompetent nature of the soluble salts in the Hormuz Complex, Ala (1974) suggested that the thickness of the Hormuz Complex to be about 1000 m in the Zagros folded belt, but ranges from 525 m to as much as 2285 m in the cores of anticlines in southwestern Iran. However, due to the lack of available seismic and drilling data, the exact limits of the thickness are not yet well defined.

3. Geology and stratigraphy of Hormuz Island

There are up to 200 salt domes (Gansser, 1992; Bosak et al., 1998; Ghazban and Al-Aasm, 2010) in the Persian Gulf, but few of them are associated with considerable banded iron salt formations (Fig. 3A and Table 1). The circular Hormuz island with a diameter of about 7 km, covers an area of 42 km² and is situated at about 24 km southeast of Bander Abbas in Hormuzgan province, Persian Gulf between 56° and 57°E and 26° and 27°N (Fig. 3A, B). Fig. 3B gives a simplified geological map of the Hormuz Island. Due to the mechanism of salt piercement, incompetent nature of rock salt and deformation during salt extrusion, it is difficult to reconstruct a normal stratigraphical relation for volcanic, volcano sedimentary and rock salt sequences. This is because of the chaotic masses of synsedimentary hematite-rich rhyodacitic-rhyolitic rocks, white rhyolitic tuffs, red sandstones and shales, banded anhydrite-hematite, foetid carbonates, cherty to jaspilitic foetid dolomite, and banded hematite-salt rocks, which dip outwards at an angle of 50–80° (Stocklin and Setudehnia, 1991). However, a possible stratigraphic column is illustrated in Fig. 3B. Geomorphologically, the Hormuz Island consists of several hills with a maximum relief of about 200 m above sea level. The most important geological units of the Hormuz Complex may be described as below:

3.1. Precambrian metamorphic basement rocks

The metamorphic basement rocks are not exposed in the Hormuz Island, though Kent (1979) and Smith (2012) reported exotic blocks of metamorphic rocks (garnetiferous schist, metamorphosed mudstone, schist and migmatite) that are assumed to have been derived from the Pan-African metamorphic basement or metamorphic Arabian shield. This study shows that these rock fragments are not exotic blocks, but actually include glaciogenic
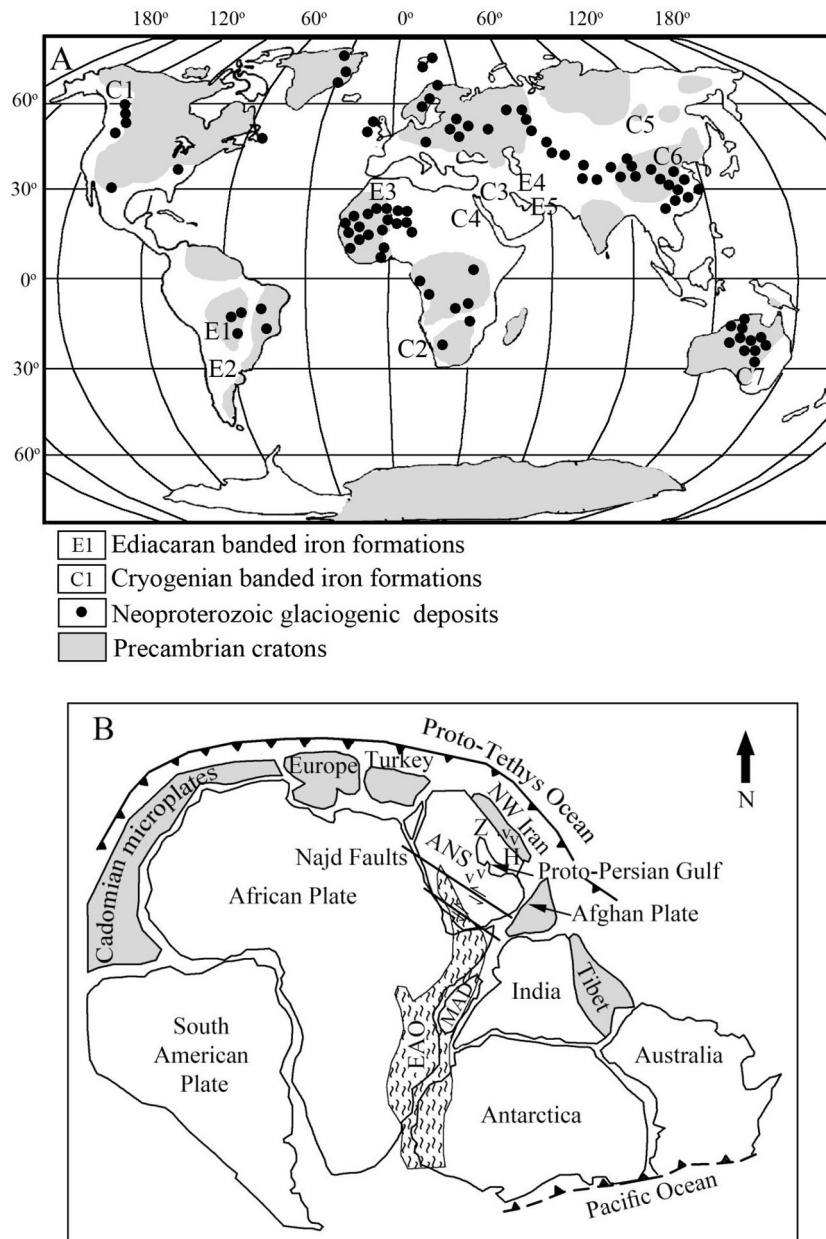
Fig. 1. A. Global position of some Cryogenian and Ediacaran banded iron formations, including Hormuz and Bafq iron ores of Iran (Modified from Klein and Beukes, 1993; Basta et al., 2011; Mohseni and Aftabi, 2015). C1 = Rapitan (755–730 Ma), E1 = Urucum (600 Ma), E2 = Yerbal (600–590 Ma), E3 = Menhouhou (630–570 Ma), C2 = Damara (750–700 Ma), C3 and C4 = Sawawin (750 Ma), E4 = Bafq (635–547 Ma), E5 = Hormuz (558 Ma), C5 = Erzin (767 Ma), C6 = Yangtze (740 Ma), C7 = Adelaide (750–700 Ma). B. The geostructural position of the Iranian microplate in the Gondwana supercontinent during the Late Neoperoterozoic (Modified from Kroner and Stern, 2005; Horton et al., 2008). H = Hormuz Island, Z = Zagros zone, EAO = East African Orogen, ANS = Arabian-Nubian Shield, MAD = Madagascar, VV = Felsic volcanism.

fragments and dropstones formed by ice melting during Ediacaran interglacial time. Certainly, these glaciogenic fragments indicate a metamorphic basement provenance, covered by the non-metamorphosed Ediacaran Hormouz Complex, although, thus, no exposures of the metamorphic basement have been observed around the Hormuz Island. In this regard, Husseini (1988) reported that all the Hormuz-type salt deposits in the Persian Gulf and the Arabian Peninsula were deposited unconformably on the eroded basement of the Pan-African metamorphic shield.

3.2. Neoproterozoic Hormuz Complex

The Neoproterozoic complex may include the five following sequences:

3.2.1. Volcanic and volcanoclastic rocks

These occur as rhyodacitic-rhyolitic pyroclastic tuff cones and cryptodomes. There are almost 25 bodies of volcanic and volcanoclastic felsic rocks that are exposed and raised above the rock salts in the Hormuz Island (Fig. 4A, B). The diameter of each body ranges from 0.5 to 1.5 km. The pyroclastic tuff cone is shaped by extrusion of the early subaqueous gas-rich felsic magma. This is reflected as the proximal near vent area and is composed of hyaloclastite breccias, sand sized hyaloclastites and rhyolitic tuffs. The occurrence of salt minerals within the sand sized hyaloclastites and tuffs indicate a synchronous shallow subaqueous felsic eruption and salt deposition. The proximal pyroclastic tuff cone is later intruded by rhyodacitic-rhyolitic cryptodomes and lava flows that are only exposed by faulting in some places. The distal zones are formed within grabens and are characterized by fine-grained tuffa-
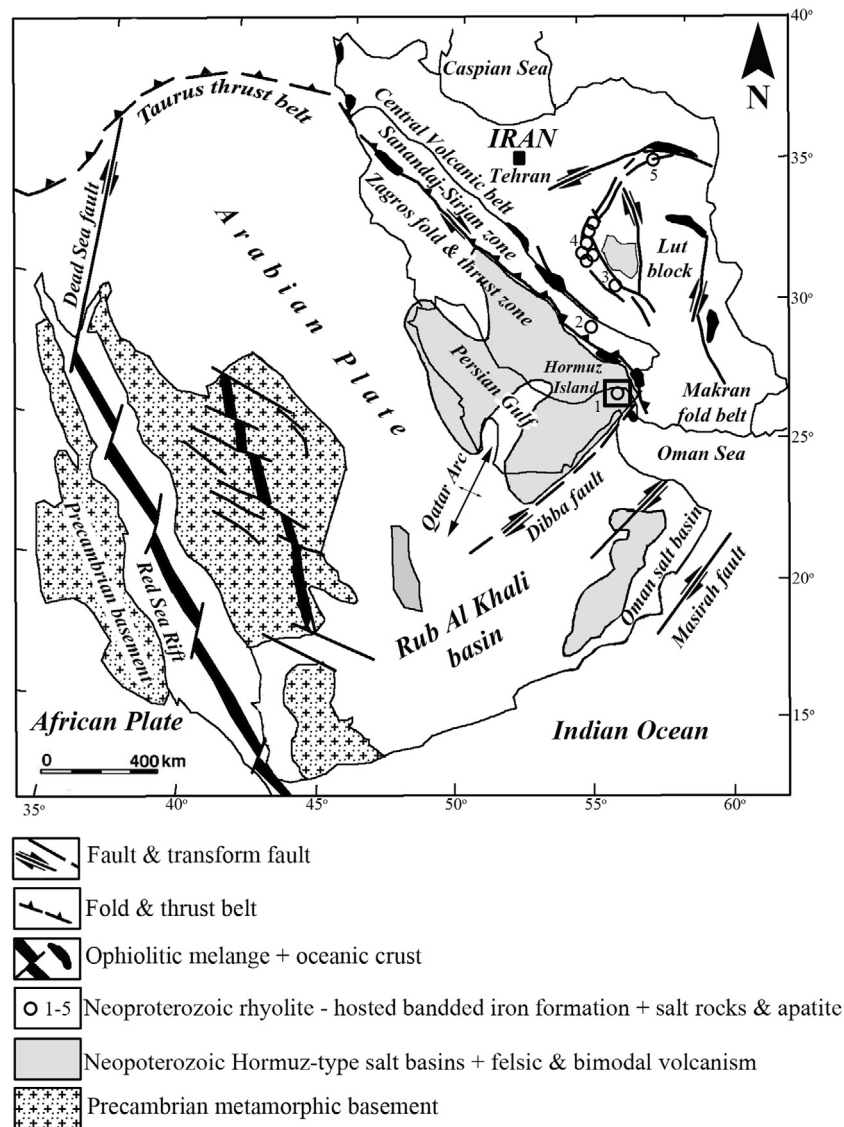
Fig. 2. Geostructural map of the Middle East, showing the Hormuz-type salt basins (Modified from Stocklin, 1968; Marzouk and El-Sattar, 1994; Ghazban, 2009; Smith, 2012). The numbers 1–5 indicate the approximate position of the Neoproterozoic Iranian BIFs. 1 = Hormuz, 2 = Gol Gohar, 3 = Jalalabad, 4 = Bafq district and 5 = Taknar area.

ceous sediments, minor carbonate rocks, salt rocks and jaspilitic banded iron formation, away from the proximal tuff cone. The presence of rhyolitic tuffs associated with rock salts, banded jaspilitic hematite (Fig. 4C), and the absence of the contact metamorphism in sedimentary rocks indicates that the felsic submarine volcanism was active during deposition of banded iron salt formation. This association is inconsistent with the genetic model of the Hormuz rhyolites as "rhyolitic enclaves" (Faramarzi et al., 2015, page 204, line 10). In fact, the enclaves form as small (<1 m) spheroidal igneous bodies that are compositionally different from their coeval lava or intrusive rocks (Bacon, 2011). The occurrence of spilitic basaltic pillow lavas in most of the Persian Gulf salt plugs (Kent, 1979) is another indication of riftogenic submarine volcanism. In the Hormuz Island, there are also minor sporadic patches of trachytes and andesites.

The exact age of rhyolitic volcanism is controversial, but Stocklin (1968) and Aghanabati (2004) suggested an age of Neoproterozoic-Early Paleozoic for rhyolitic rocks. Hurford et al. (1984) considered the hematite-apatite mineralization in rhyolitic tuff cones to be of Upper Precambrian age. Recently, valuable concordant U-Pb dating on zircons in rhyolites is reported to be about 558 ± 7 Ma (Faramarzi et al., 2015), which correlates with the Ediacaran time. In addition, Kent (1979) reported extensive quartz dioritic bodies and Alavi (2004) mentioned the occurrence of a 547 Ma leucogranitic intrusion in the western part of the Hormuz Island.

3.2.2. Sedimentary rocks

The sedimentary rocks occur as coarse-grained red micaceous sandstones, chaotic mass of feotid basal carbonates, banded iron salt formations (jaspilitic hematite), and cap carbonate.

3.2.2.1. Basal clastic rocks. The basal part of the Hormuz complex is not yet well exposed, though some possible occurrences of the coarse-grained red micaceous sandstone, shale and dolomite have been noted by Hurford et al. (1984) and Stocklin and Setudehnia (1991). The presence of micas in the red sandstones may indicate the provenance of the precursor Mesoproterozoic schists. The red sandstones are covered by thin siliclastic tuffaceous sediments. The red micaceous sandstones may be equivalent to the basal conglomerate, sandstone and dolomite of Chah Benu (Fig. 3A) salt dome in the 150 km northwest of the Hormuz salt dome (Kent,
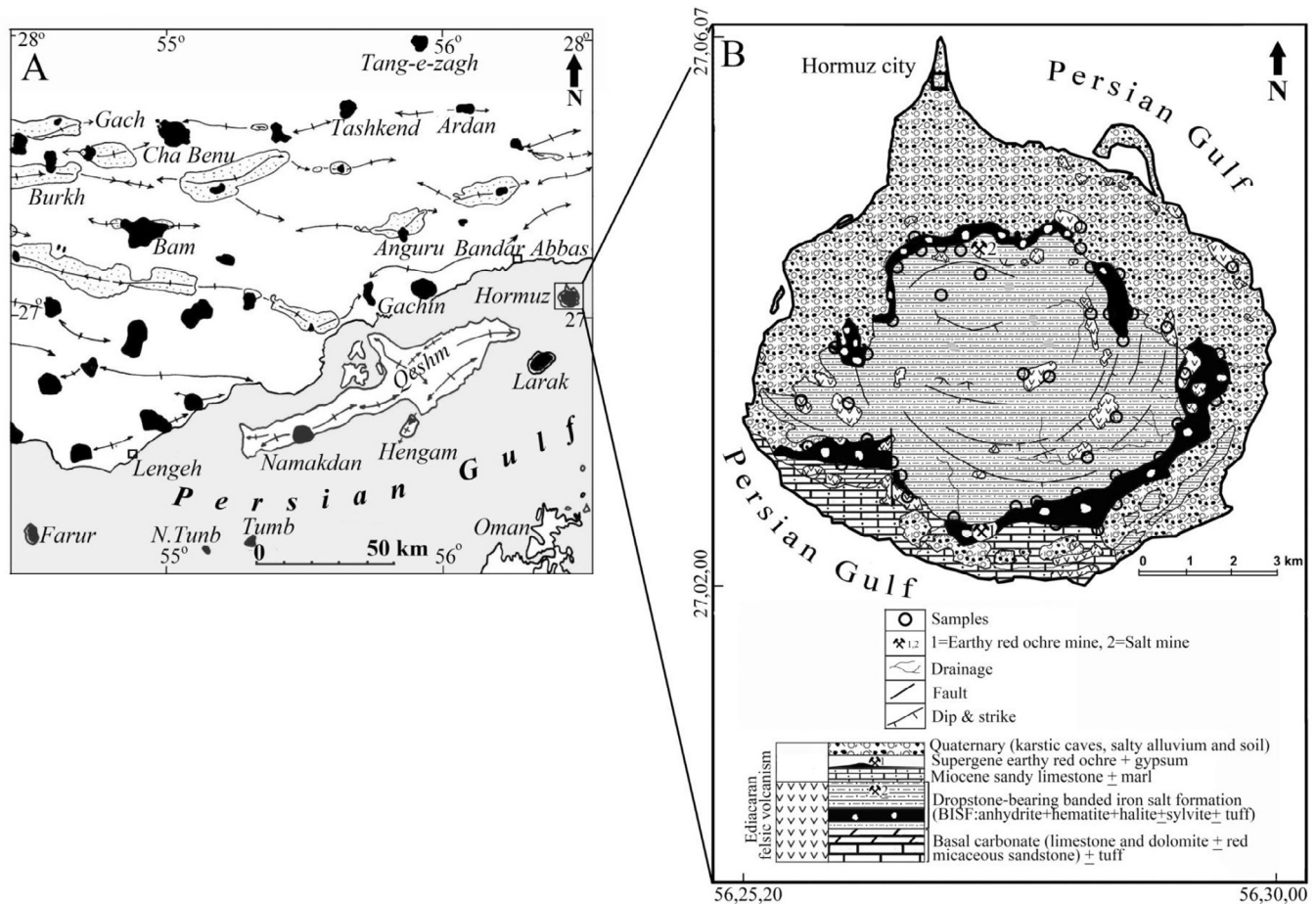
Fig. 3. A. A simplified geological map of salt domes in the Persian Gulf. B. A simplified geological map of Hormuz Island (Modified from Hurford et al., 1984; Gansser, 1992; Atapour and Aftabi, 2012).

Table 1
Summary of the most important Hormuz-type Ediacaran BISF with approximate distance away from Bandar Abbas, Persian Gulf, southern Iran (Modified from Jafarzadeh et al., 1996; Aftabi, 2001).

Deposit	Host rocks	Tonnage (million tonnes)	Grade (Fe%)
Namakdan, Gheshm (100 km southeast)	Rhyolitic tuffs and salt rocks	1	42
Larak (27 km south to southeast)	Rhyolitic tuffs, salt rocks and marl	3	45
Tang-e Zagh (110 km north – northwest)	Rhyolitic tuffs, salt rocks and dolomite	6	55
Tashkend (100 km northwest)	Ryhyolitic tuffs, salt rocks and dolomitic limestones	1	58
Ardan (85 km north-northwest)	Rhyolitic tuffs, salt rocks and dolomite	1	38
Gachin (50 km west	Rhyolitic dome, tuffs, salt rocks and dolomite	1	46.4
Farur (268 km southwest)	Rhyolitic dome, tuffs, salt rocks and dolomitic limestone	0.25	64

1979), the Rizu Formation (Houshmandzadeh et al., 1988) and also similar to the basal part of the Ediacaran Oman rock salts (Smith, 2012).

3.2.2.2. Basal carbonate rocks. The basal part of the evaporite sequences starts with carbonate rocks (Warren, 2006, 2012). The Hormuz carbonates are the most frequent basal rocks of the salt rocks and occur as brown to yellowish foetid finely laminated carbonate rocks and contain minor thin layers of tuffaceous sediments. The carbonate rocks may be equivalent to that of Soltanieh dolomites of the Alburz regions, northern Iran. The fine lamination and foetid nature of the carbonates may indicate deposition in algal mats. These dolomitic carbonate rocks contain

Spriggina bearing concentric algae discs of the Neoproterozoic-Early Cambrian (Kent, 1979). Basal carbonate rocks are also reported on basement of Ghaub Formation, Namibia. Similar Spriggina bearing carbonatic rocks have been reported in the Fe-P Bafq mining district by Forster and Jafarzadeh (1994), but were explained to be of Ediacaran-type fauna by Mohseni and Aftabi (2015).

3.2.2.3. Jaspilitic banded iron salt formation (BISF). This is the most extensive volcano-sedimentary exhalative formation that covers the basal carbonate rocks. The mineralization occurs in proximal and distal zones. The proximal mineralization is not extensive and is mainly composed of massive hematite with minor actinolite,

Fig. 4. A. Proximal and distal zones of BISF hosted by felsic volcanism. B. A closer view of proximal massive hematite ore. C. Sequences of tuffaceous felsic rocks, hematite and tuffaceous evaporates. D. Massive macrobandings of hematite ore. E. Typical rhythmic mesobandings of tuffaceous jaspilitic hematite-salt minerals. F. Folded mesobandings in jaspilitic hematite. G. Mesobandings in hematite (black) and anhydrite-carbonate (white). H. Microbandings in layered hematite and halite.

apatite, tourmaline, chlorite, albite and sericite. (Fig. 4A, B, D). The ore has an average thickness of about 1.5 m and extends to 10–50 m down dip within the proximal zone of the rhyolitic tuff cone. The distal zone occurs as a sequence of rhyolitic tuffs and extensive banded tuffaceous jaspilitic-hematite-anhydrite-halite-sylvite with minor chlorite, carbonates, sericite and clay minerals (Fig. 4C, E, F, G, H). The ore extends to about 8 km in length with an average thickness of 300 m, although Ala (1974) gives a thickness of about 525 m. However, the thickness varies considerably due to local dissolution of salt minerals and karstification. The most peculiar feature of this unit is the occurrence of a peripheral ring of glaciogenic dropstone-bearing and diamictite-rich jaspilitic banded iron formation in the Hormuz Island. An active mine of red brown ocher, known colloquially as Persian red is formed by supergene oxidation and karstification. The rock salt is white, dull grey to red with coarse-grained texture and in some places shows red karstified features due to the hydration and dissolution of hematite and salts.

3.2.2.4. Cap carbonate. Cap carbonate defines the upper stratigraphic unit of the Neoproterozoic sequences at Hormuz Island and is exposed as a thin discontinuous layer over the jaspilitic banded hematite-salt rocks. Due to the contorted nature of the Hormuz Complex (Ala, 1974; Stocklin and Setudehnia, 1991), dissolution and karstification of the underlying salt rocks, the thickness of cap carbonate varies greatly and has been reported to be 1 to 50 m thick in places (Ahmadzadeh-Heravi et al., 1990; Hoffman et al., 2011; Wen et al., 2015). The cap carbonate at Hormuz Island is composed of dark to dark-grey or buff foetid cherty-shaley dolomitic carbonates with rhythmic lamination, probably due to the microbial mats (Ahmadzadeh-Heravi et al., 1990; Kimura et al., 1997; Ghazban and Al-Aasm, 2010). So far, no significant banded tuffaceous hematite-salt rocks have been observed in cap carbonates, except very minor amounts of fine-grained halite inclusions in dolomitic carbonates. The occurrence of stromatolites, in particular the genus Collenia and Conophyton sp of Upper Precambrian (Ediacaran time) has been reported in carbonates of several Persian Gulf salt domes, including the Hormuz salt rocks (Kent, 1979).

3.3. Miocene formation

The Miocene Formation starts with a thin layer of conglomerate, covered by sandy limestone, green silty marlstone and shale, which may be considered as an equivalent to the Upper Fars Formation in other parts of the Zagros structural zone.

3.4. Pliocene-Quaternary sequences

These units include sandy conglomerate and sandy limestone of Pliocene, covered by coral reef limestones of Pleistocene, recent alluvial terraces, sand dunes, clastic beach deposits and salty alluvium and soil, respectively.

3.5. Sampling and analysis

Due to the small area of the Hormuz Island and very monotonous nature of rock types, only about 45 samples were collected from the surface outcrops. Samples of 1–2 kg were taken from fresh rhyolite, altered rhyolite, the banded jaspilitic rock, rock salts, diamictite, dropstones and cap carbonate. Furthermore, because of the presence of dangerous salt caverns, it was not always possible to maintain a uniform sample density. However, sample intervals were spaced at about 0.5–2 km. Rock samples were cut and thin and polished sections were prepared and subsequently investigated by optical microscopy at the Department of Mining Engi-

neering, Shahid Bahonar University of Kerman. The loss on ignition (LOI) was calculated by heating the oven dried samples at about 1100 °C in a furnace for an hour, and measuring the weight loss as weight percent. Powdered rock samples were digested by aqua regia and analysed by ICP-OES and ICP-MS methods for major oxides, minor and precious elements and REE at the laboratories of the SGS Mineral Services and ALS Chemex, Canada. According to the Reference Standard Materials of SGS, the accuracy for different elements ranged from 1 to 10%. Table 2 gives limits of detection, chemical composition of felsic rocks and precision for a repeated sample of rhyodacite.

4. Ore structure and petrography of the banded iron salt mineralization

Iron-salt mineralization at Hormuz and other Persian Gulf Islands has several structural relations in common:

1- The first form of iron mineralization occurs as proximal massive hematite associated with rhyodacitic-rhyolitic tuff cone (Fig. 4A, B, D).
2- The second and the most frequent mode of banded iron salt mineralization forms banded hematite and salt rocks in distal zone around the rhyodacitic-rhyolitic tuff cone and tuffaceous rhyolite (Fig. 4A, C, E).
3- The third occurrence of iron mineralization is represented by specularite hematite-salt minerals, indicating typical BIFs macrobanding, mesobanding and microbanding layers in distal zone of rhyodacitic-rhyolitic tuff cone (Fig. 4D, E, F, G, H).
4- The fourth type of iron mineralization forms the banded hematite-apatite ore (Fig. 5A).
5- The fifth form of iron mineralization occurs as residual supergene earthy red brown goethite-hematite (Fig. 5B) and also as mesobandings of halite and hydrated hematite (Fig. 5C). The red ocher goethite-hematite is currently mined
6- The sixth type of iron salt mineralization occurs as dropstone and diamictite-bearing jaspilites and banded hematite-salt layers in the distal zone (Fig. 5 D, E, F, G, H).

Hematite and apatite also form very minor vein-type mineralization. The frequent field occurrence of red color in salt rocks, rhyolitic tuffs and other sedimentary rocks is related to the very fine bands of red hematite. This indicates that rock salt sedimentation, rhyolitic volcanism and iron mineralization occurred syngenetically and synchronously. In this regard, Kent (1979, page 126) reported simultaneous sedimentation of evaporites, tuffs and volcanogenic sediments at Hormuz Island.

The most significant structural features are related to the diamictite and dropstone bearing hematite-salt minerals (Fig. 5D, E, F, G, H). The pebbles are polygenetic, heterogeneous and are composed of sericite, epidote, cherty dolomitic marbles and metamorphosed mudstones. The dropstones also occur in most of the salt plugs of the Persian Gulf, but have been misinterpreted by previous studies. Player (1969), Kent (1979), and Smith (2012) considered inclusions of slate, schist, migmatite, metamorphosed mudstone, olistostrome and gneissic granite as metamorphic xenoliths or exotic blocks of the metamorphic basement to have fallen from fault scarps. The dropstones of glaciogenic origin occur as bullet-shape (Hoffman et al., 1998; Gaucher et al., 2015; Le Heron et al., 2017). The presence of bullet-shape dropstones and metamorphosed mudstones (Fig. 5 D, E, F, G, H) shows that these fragmental rocks are of glaciogenic origin. Moreover, some salt-bearing dropstones show ripple marks, pointing to a shallow glaciomarine deposition (Fig. 5H). To explore the precise composi-

Table 2

Detection limit, major (wt%), minor (ppm) and precious (ppb) elemental contents of fresh (FR-1), altered (AR-1) felsic rocks and precision of a repeated rhyodacite (FR-6) sample.

Elements	Detection limit	FR-1	FR-2	FR-3	FR-4	FR-5	AR-1	AR-2	AR-3	AR-4	AR-5	AR-6	AR-6	Precision (%)
SiO_2	0.01%	71.6	69.5	73	69.7	70.3	67.3	67.9	68.6	67.8	68.1	67.9	68.3	99.6
TiO_2	0.01%	0.31	0.29	0.4	0.4	0.27	0.34	0.33	0.32	0.28	0.36	0.42	0.43	98.4
Al_2O_3	0.01%	12.3	13.4	13	12.2	13.5	11.7	11.5	12.4	12.1	11.8	11.6	11.5	99.4
Fe_2O_3 (total)	0.01%	3.48	4.54	3.4	5.65	4.68	7.73	4.5	6	5.5	6.5	8.18	8.25	99.4
MnO	0.01%	0.08	0.07	0.1	0.09	0.05	0.04	0.07	0.04	0.05	0.05	0.01	0.01	100
MgO	0.01%	0.49	0.48	0.5	0.61	0.58	2.53	1.04	0.61	0.83	1.21	2.04	2.06	99.3
CaO	0.01%	1.88	2.1	1.2	1.46	1.2	0.36	0.1	0.7	1.1	0.31	0.1	0.1	100
Na_2O	0.01%	3.9	2.25	3.1	2.46	2.61	1.5	5.42	6.6	6.4	1.4	2	1.7	97.5
K_2O	0.01%	4.79	4.68	4.5	4.61	4.42	3.22	2.23	0.68	0.78	3	4.17	4.14	99.5
P_2O_5	0.01%	0.05	0.04	0.1	0.09	0.08	0.09	0.07	0.08	0.07	0.08	0.07	0.07	100
LOI	0.01%	0.79	1.87	0.7	1.89	1.68	4.81	3.93	3.96	4.63	7.1	2.93	3.2	98
Total	–	99.6	99.7	99	99.2	99.2	99.6	99.2	100	99.54	99.58	99.42	99.33	–
Ba	10 ppm	900	834	884	790	745	980	954	890	790	826	60	70	98.8
Cs	0.1 ppm	0.8	0.5	0.8	0.4	0.3	0.2	0.6	0.5	0.4	0.5	0.9	0.9	100
Cl	50 ppm	46	43	54	41	58	70	50	42	90	121	50	50	100
Co	0.5 ppm	1.7	4	2	2.2	1.8	5	7	3	4	6	1.2	1	87.3
Cu	5 ppm	24	21	22	28	25	51	48	13	36	41	13	15	90
F	20 ppm	22	27	31	<20	23	37	40	43	52	57	20	20	100
Ga	1 ppm	26	24	22	21	25	27	24	23	19	24	23	23	100
Au	5 ppb	<5	<5	<5	5	<5	5	6	5	5	5	5	6	77
Hf	1 ppm	6	4	3	5.3	4.8	7	5	8	4	6	6	7	90
Mo	2 ppm	2	3	<2	2	2	4	3	2	2	3	5	5	100
Ni	5 ppm	6	7	5	5	<5	6	6	4	8	9	5	6	87.3
Nb	1 ppm	24	27	23	25	26	27	25	19	28	29	11	11	100
Pd	5 ppb	<5	<5	<5	6	5	5	5	5	7	6	5	5	100
Pt	10 ppb	<10	<10	<10	10	<10	10	<10	10	10	12	10	10	100
Rb	0.2 ppm	146	132	152	149	140	91.7	102	98	74	110	175	179	98.4
Ag	1 ppm	1	<1	1	2	1	3	2	1	3	4	1	1	100
Sr	10 ppm	150	125	138	126	130	60	80	67	66	70	52	57	99.3
Ta	0.5 ppm	0.9	0.7	0.6	0.8	0.5	0.8	0.5	0.9	0.9	0.7	0.6	0.7	99.2
Th	0.1 ppm	12.8	14	12	12.7	11	12	12.6	10	10	14	8	6	80
Sn	1 ppm	1	1	<1	1	1	1	2	1	2	1	6	7	99.8
W	1 ppm	2	3	2	2	<2	3	4	<2	<2	2	2	4	89.2
V	5 ppm	30	32	27	25	20	24	29	19	22	36	31	30	97.7
Zn	5 ppm	10	16	14	18	20	24	22	26	25	21	5	7	77
Zr	0.5 ppm	247	210	268	256	324	270	236	242	228	240	223	235	96.4
La	0.1 ppm	34.8	32	32	32	35	41	45.4	38	29	40	51.5	55.7	94.6
Ce	0.1 ppm	71	65	70	68	72	82	78	76	74	77	71.6	74.1	97.6
Pr	0.05 ppm	8.1	7.2	7.5	6.45	7.1	8	5.8	7.9	6.4	7	5.9	6.3	95.1
Nd	0.1 ppm	29	25.6	25	26	27	30	32	34.2	31.5	34	17.4	18.1	97.2
Sm	0.1 ppm	6	5.2	6.8	7.2	7	8	9	7.6	8.5	7.8	2	2.2	93.4
Eu	0.05 ppm	0.68	0.56	0.6	0.7	0.64	0.8	0.86	0.75	0.78	0.75	0.46	0.5	93.7
Gd	0.05 ppm	5.68	5.48	4.8	5.1	5	6	7.1	6.5	7	6.8	4.17	4.10	95.6
Tb	0.05 ppm	0.94	0.91	0.8	0.8	0.7	0.97	0.75	0.9	1	0.8	0.63	0.63	100
Dy	0.05 ppm	7.8	8.1	8.5	8.6	8	9	9.4	8.5	9.6	7.6	6.63	6.85	80
Ho	0.05 ppm	1.7	1.64	1.8	1.8	2	2.3	2.6	2.1	2.4	2.5	2.0	1.9	96.4
Y	0.5 ppm	30	52	49	47	51	58	54	46	50	55	42	45	95.1
Er	0.05 ppm	5.32	6.3	6.1	6.5	6	7	5.8	5.5	7.5	6.5	4.46	4.51	92.7
Tm	0.05 ppm	0.97	6.4	0.9	1	0.94	1.2	1.3	0.96	0.9	0.8	0.81	0.82	94
Yb	0.1 ppm	5.76	5.92	6	6.7	6.3	7	7.6	5.5	7.4	6.6	4	4	100
Lu	0.05 ppm	0.86	0.91	0.8	0.9	0.86	1	0.97	0.95	0.8	0.9	1.14	1.17	87

tion of dropstone requires evidence of clast striations, but these structures may not have been preserved due to the structural deformation and salt extrusion that affected some of the BIFs worldwide (Ali et al., 2010; Mohseni and Aftabi, 2015). Also, as the dropstones could not be easily separated from their matrix, it is difficult to verify the presence of the sharper point striations of the clasts.

4.1. Petrography

Rhyodacitic-rhyolitic tuff cones and domes are the most common host rocks to iron mineralization. They are composed of phenocrysts of quartz and sanidine in a fine-grained alkali feldspar, quartz and or glassy matrix. Fresh plagioclase (oligoclase) occurs less frequently, though albite is formed by albitization due to the seawater reaction with felsic magma. Mafic minerals are secondary amphibole and biotite, though minor primary euhedral biotite

flakes are also observed. Some secondary or hydrothermal biotites display very pale orange-colorless pleochroism, possibly similar to that of phlogopite or Mg-biotite. This is due to the removal of magnesium ion from seawater, reaction with primary biotite, and formation of Mg-biotite during hydrothermal alteration. This seems likely as the altered rhyolites at Hormuz Island are enriched in MgO up to 2.53%. Hydrothermal phlogopite has been reported to occur in altered rhyolite from Mnanka, North Mara, Tanzania (Kavana, 2015). Mg-biotites formed by hydrothermal alteration and are not reliable for the tectonomagmatic discrimination diagrams. It is notable that the common biotite in felsic volcanic rocks is Fe-rich biotite (Deer et al., 1977). The most typical alteration minerals occur as tourmaline, apatite, chlorite, sericite, epidote, actinolite and albite. The mineralogical compositions of rhyolite and rhyodacite are similar to the felsic rocks given in Clemens et al. (1986) for A-type rhyolite. Actinolitization, albitization, chloritization and apatitization mainly occur in the proximal zone of
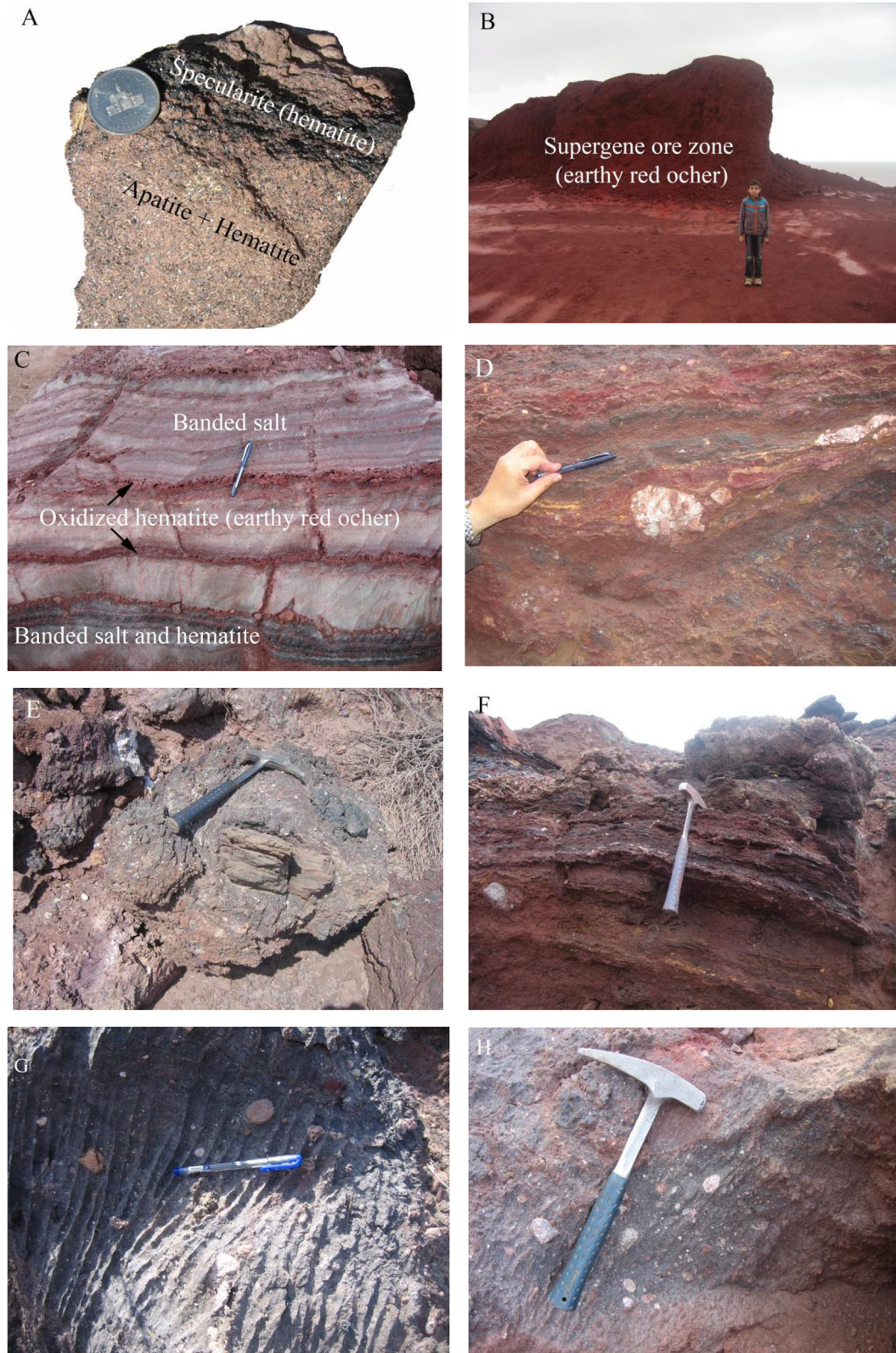
Fig. 5. A. Banded hematite-white apatite crystals. B. Residual supergene earthy red ochre (goethite and hematite). C. Mesobandings of halite-rich bands interlayered by microbandings of hydrated hematite and epigenetic hydrated hematite veins. D. Quasi bullet-shape and subrounded dropstones in banded jaspilitic hematite, deflecting the jaspilitic bands. E. A meta-limy mudstone and some rounded dropstones in banded hematite-halite. F. Rounded and bullet-shape dropstones in banded hematite and salt minerals. G. Subrounded-rounded dropstones in weathered ripple mark-bearing salt minerals. H. Bullet-shape dropstones in salt minerals and hematite.

hematite mineralization. Tourmalinization is associated with apatite and hematite mineralization, by replacing biotite, sanidine and oligoclase (Fig. 6A, B). The tourmaline crystals show pleochroism from yellow, brown or blue to yellowish green, which correlate with iron–rich tourmaline, probably schorl or foitite. Slack and Trumbull (2011) reported Fe and Al–rich tourmaline association with rhyolitic rocks. This alteration assemblage is also reported in some banded iron formations (Thompson and Thompson, 1996; Mohseni and Aftabi, 2015). Tourmalinization is possibly developed by interaction of B, Fe, Mg, Si and P-rich fluids with aluminum bearing permeable sediments or hyaloclastite volcanic rocks at (200–400 °C) and pH of 6–8 (Slack, 1993) in banded iron formations. Sericitization and epidotization are also associated with hematite mineralization (Fig. 6C). Chloritization occurs as replacement in the structure of plagioclase and ferromagnesian minerals. They occur as greenish euhedral iron-rich chlorites, probably ripidolite, and show the interference color of bluish to purple with pale-yellowish pleochoism in proximal zone. Exhalative chlorites are reported to form at about 350 °C (Tivey, 2007). Minor chlorite grains are also formed in distal zone, indicating anomalous interference colors with pale green to colorless pleochroism and resemble clinochlore.

Anhydrite, gypsum and halite occur in fractured rhyolitic hyaloclastites and tuffs. Opaque minerals include hematite with very minor amounts of pentagonal and dodecahedral pyrite.

4.2. Mineralogy

Mineralogical studies indicate that most of the minerals show at least two generations:

4.2.1. Hematite
Hematite shows several structural and textural varieties. The first type of hematite mineralization occurs as massive hematite ore in the proximal zone of the rhyodacitic-rhyolitic tuff cone (Fig. 4D).The second generation forms nodular hematite and chert (jasper) in a matrix of tuffaceous layered salt minerals that indicate early diagenetic stage of mineralization (Fig. 6D).The third generation of hematite forms microbanding with jaspilite (Fig. 4F and Fig. 5D). Klein and Beukes (1993) and Baldwin et al. (2012) also found similar diagenetic nodular hematite–jaspilite associations in glaciogenic banded iron formations. Type 4 of hematite occurs as very thin epigenetic veins or flakes, crosscutting the banded salt minerals and hematite-chert (Fig. 5C). The banded hematite-chert layers also show arching caused by dropstones (Fig. 6E). In rare cases, hematite forms alignment inclusions in salt minerals, in particular halite, which gives a dark grey to red banding in the banded iron salt formations. The presence of primary hematite in halite grains has also been indicated by Houghton (1980). Under the reflected light, hematite grains show distinctive anisotropism (bluish grey to yellowish grey) and banded texture (Fig. 6F).

4.2.2. Anhydrite
Anhydrite occurs as the most frequent primary sulfate minerals in banded iron salt formations, shows mesobanding with hematite and halite (Fig. 4G) and is composed of fine-grained crystals that are replaced by gypsum.

4.2.3. Gypsum
Gypsum is a secondary sulfate that replaces anhydrite and forms rimmed texture around it due to the karstification and hydration.

4.2.4. Halite and sylvite
Halite is the most frequent primary salt minerals at Hormuz Island and is composed of coarse-grained granular (1–12 mm)

crystals that contains several inclusions of hematite. The crystals show white, red and grey color and occur within banded hematite and anhydrite bands (Fig. 4E, G, H). Secondary halite forms stalactites and globular crystals in caves due to dissolution and karstification of the primary halite. Very minor sylvite grains with bitter taste have been observed with halite, in particular in the eastern part of the Hormuz Island.

4.2.5. Dolomite
Dolomite forms as dark-grey and coarse-grained (1–20 mm) euhedral crystals in basal carbonate units and also occurs as dark to buff crystals in cap carbonates that contains inclusions of halite crystals.

4.2.6. Apatite
Apatite forms three textural generations. The first type shows fine-grained subhedral to euhedral crystals in altered rhyolite. The second generation of apatite is coarse-grained (1–10 mm) and frequently associated with banded hematite (Fig. 5A, Fig. 6A, B). Exceptional and very coarse-grained vein-type greenish apatite crosscut the banded hematite and has been seen in residual supergene earthy red ochre mine.

4.2.7. Pyrite
Pyrite occurs as a minor sulfide mineral in dark shaley dolomite that shows fine-grained texture (1–5 mm) as well as very large pentagonal crystals (1–3 cm).

4.2.8. Other minerals
Minor and very fine-grained rounded zircon, monazite and quartz grains have been observed in cap carbonates and banded hematite-salt rocks. Fig. 7 gives a possible paragenetic sequence at the Hormuz banded iron salt formation.

5. Geochemistry

The geochemical results for major, minor, precious and REE elements in rhyodacite-rhyolite, BIFs, hematite-rich diamictite, dropstone, halite and cap carbonates are given in Tables 2–4, respectively.

5.1. Rhyodacite-rhyolite

According to Table 2, the SiO_2 values in rhyodacites-rhyolites range from 67.3 to 73%, which is higher than the average content of fresh rhyodacite (65.55%), but close to the average of fresh rhyolite (72.82)%, proposed by Cox et al. (1979). The Fe_2O_3 (4.50–7.73%), MgO (0.61–2.53%) and LOI (3.93–7.1%) contents of the hydrothermally altered rhyolites at Hormuz Island are almost 2 to 9 magnitudes higher than the fresh continental A-type rhyolitic-rhyodacitic rocks (McClellan and Gazel, 2014). The high values may be related to the reaction of subseafloor hydrothermal fluids with felsic magma during submarine volcanism. This is approved by experimental work of Hajash and Chandler (1981), who showed that considerable Mg enrichment occurred in altered rocks by interaction of seawater with felsic magmas. Na_2O and K_2O show some variations due to sericitization, albitization and argillic alteration. The other minor, trace and precious elements are within the background values in fresh felsic rocks.

In order to explore the petrogeochemical and tectonogeochemical nature of the felsic rocks, SiO_2-Zr/TiO_2 (Fig. 8A), chondrite normalized REE + Y patterns (Fig. 8B), Zr-10000 × Ga/Al (Fig. 8C), Nb-10000 × Ga/Al (Fig. 8D), Y-Nb-Ce (Fig. 8E), Rb/Nb-Y/Nb (Fig. 8 F), Zr-TiO_2 (Fig. 8G) and Rb-Y + Nb (Fig. 8H) diagrams were used. The results indicate that felsic rocks of the Hormuz Complex plot
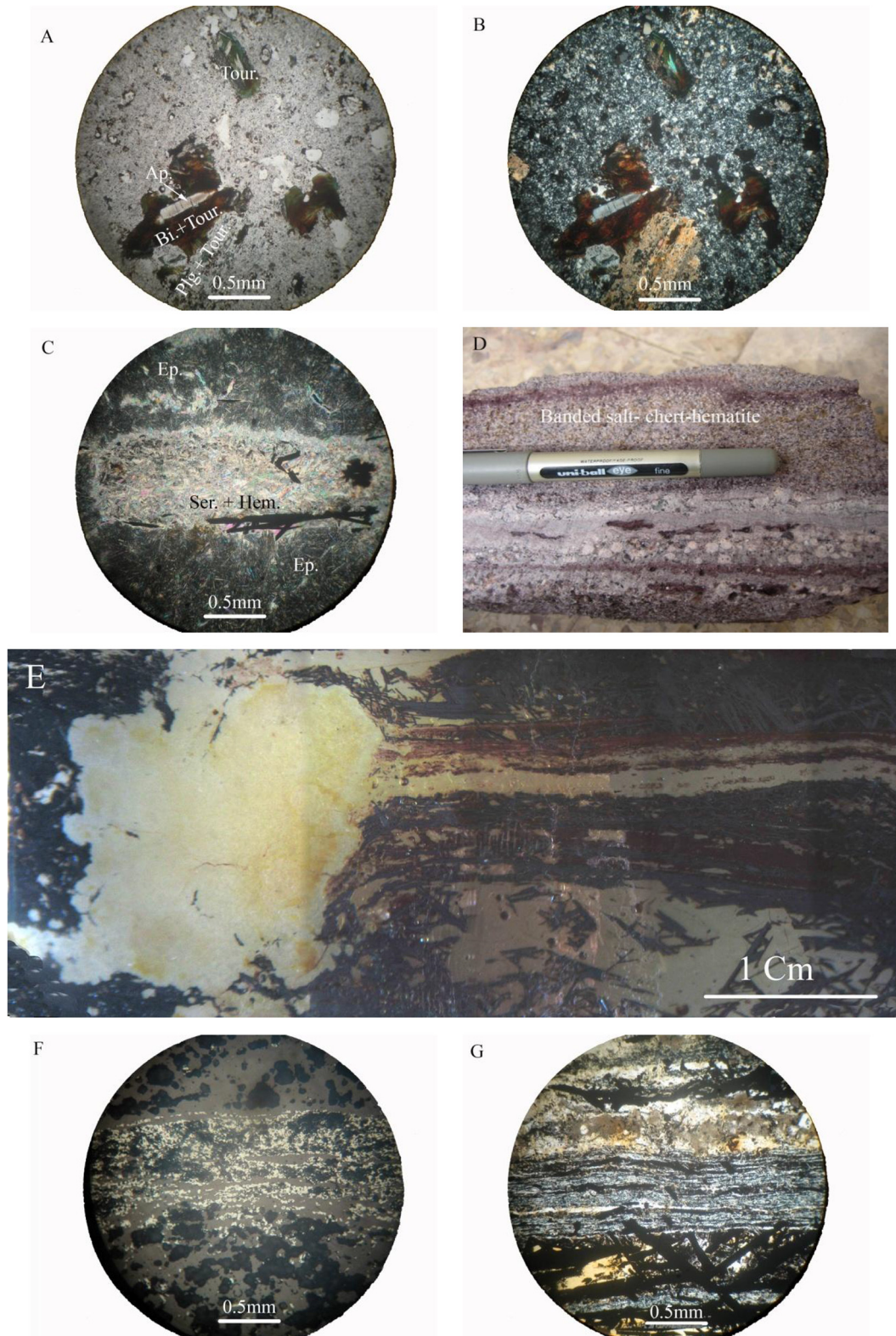
Fig. 6. A. and B. Tourmalinized and apatitized rhyolite, polarized light (A) and crossed nicols (B). C. Epidotized and sericitized rhyolite, polarized light. D. Nodular and laminated chert-hematite layers. E. A meta-cherty marble dropstone, arching and draping the iron oxide-silica gels during syndiagenesis. F. A microphotograph, indicating the micro-cryptobandings in hematite, reflected light. G. A microphotograph, showing the micro-cryptobandings in banded chert-hematite, crossed nicols. Tour. = tourmaline, Ap. = apatite, Plg = plagioclase, Bi. = biotite, Hem = hematite, Ser. = sericite.

within the domain of the rhyolitic-rhyodacitic rocks. They also have an affinity to the riftogenic and within plate A-type alkaline rhyolites (Fig. 8C, D, E, F, G, H) as suggested by Atapour and Aftabi (2017). The overall contents of trace elements and REE + Y (Table 2) are close to the limits of felsic rocks, though some variations might be related to the hydrothermal alteration effects. The

Minerals	Felsic Magmatism	Submarine hydrothermal alteration and mineralization	Synglaciogenic clasts	Epigenetic hydrothermal	Supergene and oxidation
Alkali feldspar (sanidine)	▬▬▬				
Quartz	▬▬▬	--------------	--------	----------	
Oligoclase	▬▬▬				
Amphibole(actinolite)		------------			
Biotite	------------	------------			
Albite		----------------			
Chlorite		----------------			
Sericite		--------------	--------		
Epidote		--------------	--------		
Tourmaline	--------------	▬▬▬			
Apatite	--------------	▬▬▬		---------	
Hematite	------------	▬▬▬		---------	
Chert		▬▬▬	--------		
Anhydrite		▬▬▬			
Gypsum					------------
Halite		▬▬▬			-----------
Sylvite		----------------			
Reddish brown goethite and hematite (Persian red)					------------
Pyrite		--------------			
Chalcopyrite		--------------			
Malachite					-------------
Zircon	------------		--------		

Fig. 7. Paragenetic sequences of mineralization at Hormuz Island.

REE + Y patterns for rhyolite-rhyodacite samples (Fig. 8B) are sub-parallel and show a V-shaped negative Eu anomaly similar to the A-type felsic rocks reported by Eby (1992, 2011). In this regard, Faramarzi et al. (2015, page 204, line 7), admitted a rift-related as well as continental arc setting for felsic volcanism. It is highly notable that, even by plotting the geochemical data (immobile elements) of Faramarzi et al. (2015), on tectonomagmatic diagrams (Atapour and Aftabi, 2017, Fig. 4), the samples plotted within the field of A-type rhyolites.

5.2. Banded iron formation, diamictite-bearing banded iron formation, dropstones and red ochre

As shown in Table 3, SiO_2 (5.56–26.33%) and Fe_2O_3 (21.0–71.7%) are the most abundant oxides at Hormuz banded iron salt formation, reflecting the mesobandings and microbandings of chert and hematite in jaspillites. The high values belong to the diamictites and dropstones-rich BIFs. In contrast to these oxides, Al_2O_3 shows low values, ranging from 0.42 to 1.2%, but higher Al_2O_3 contents are related to diamictite or dropstone-rich BIFs, which reach up to 8.6%. Similar major oxide data for glaciogenic BIFs are also given in Yeo (1981) and Klein and Beukes (1993). It is noteworthy that P_2O_5 contents are higher than non-glaciogenic BIFs, but very close to those of the glaciogenic ones reported by Ilyin (2009). Importantly, the alkali oxides, in particular Na_2O values are almost three magnitudes higher than any other reported BIFs and may reach up to 1.2%. Parallel to Na_2O, chlorine ranges from 54 to 7542 ppm. The high Na_2O and Cl concentrations are well correlated with the presence of halite-hematite microbandings and cryptomicrobandings, though the BIF samples look to be purely of hematite composition. The CaO, MgO and MnO values are low, except in diamictite and dropstone-rich samples. The volatile content (LOI)

ranges from 1.04 to 4.1% and reach up to 18.4% in diamictite and dropstone-bearing BIFs. The low values of copper (9–493 ppm) and gold (<5–8 ppb) in BISFs are close to the glaciogenic Bafq mining district (Mohseni and Aftabi, 2015) and do not match with the IOCG or Kiruna-type iron oxide mineralization.

The major oxide composition of diamictite – rich BIFs is very different from the clast-free BIFs (Table 3). They are extremely rich in CaO (12.0–55.3%), MgO (1.25–1.90%) and LOI (10.5–14.5%), but depleted in SiO_2 (5.56%), which may indicate a marble-rich provenance. Some dropstones are extremely rich in SiO_2 (48.6–52-2%), Al_2O_3 (8.14–8.60%), LOI (18.1–18.4%), CaO (11.3–12.0%) and MgO (4.16–5.20), which show similarity to the calc-silicate schist or meta-limy mudstone provenance.

Compared to the hematite-rich BIFs, the composition of supergene earthy red ochre is characterized by higher Fe_2O_3 (77.0–77.6%) and lower SiO_2 (14.4–16.2%), though strong depletion in CaO, Na_2O, K_2O and Cl is notable. In one sample of proximal ore, the Ba content (70 ppm) is ten magnitudes lower than the distal BISF (760 ppm).

Some immobile minor elements including Zr (30–162 ppm), La (18–228 ppm), Ce (24.7–282 ppm), Tb (0.29–3.1 ppm), Tm (0.05–0.8 ppm) and Y (3–28 ppm) are highly enriched in BIFs as well as diamictite-rich BIFs. These high values may indicate the inputs of these elements from the dropstones, containing detrital zircon, xenotime and monazite. Similar detrital inputs of the elements have been reported by Baldwin (2014) and Mohseni and Aftabi (2015) in glaciogenic BIFs. This is also supported by the high ratios of Y/Ho (27.5–70).

The geochemical signatures of rare earth elements (REE + Y) in banded iron salt formation can originate from hydrothermal, hydrogenous and detrital inputs. In this regard, the REE + Y distributions for banded iron salt formations and dropstones are nor-

Table 3
Major (wt%), minor (ppm) and precious (ppb) elemental contents of banded iron formation (BIF), hematite-rich diamictite, dropstones and red ochres.

Elements	BIF (distal-1)	BIF (distal-2)	BIF (distal-3)	BIF (distal-4)	BIF (proximal-1)	Hematite-rich diamictite-1	Hematite-rich diamictite-2	Dropstone-1	Dropstone-2	Red ochre-1	Red ochre-2
SiO_2	25.2	19.3	26.33	21.7	34	5.56	7	52.2	48.6	14.4	16.2
TiO_2	0.03	0.06	0.09	0.12	0.3	0.03	0.04	0.34	0.43	0.12	0.2
Al_2O_3	0.57	0.68	0.48	1.2	0.42	0.88	0.54	8.14	8.6	1.2	0.65
Fe_2O_3 (total)	71.6	71.4	70.4	71.4	61.8	21	66.5	2.82	3.5	77.6	77
MnO	0.01	0.02	0.03	0.08	0.02	0.02	0.01	0.31	0.25	0.3	0.2
MgO	0.01	0.03	0.05	0.1	0.09	1.25	1.9	4.16	5.2	0.1	0.12
CaO	0.07	0.09	0.07	0.28	0.14	55.3	12	11.3	12	0.28	0.1
Na_2O	0.7	0.96	0.68	1.2	0.3	0.1	0.2	1.5	2	1.3	0.6
K_2O	0.12	0.21	0.15	0.9	0.13	0.52	0.48	0.39	0.43	0.9	0.5
P_2O_5	0.3	0.4	0.36	0.46	0.2	0.14	0.18	0.1	0.13	0.26	0.3
LOI	1.04	4.1	1.4	3.2	2.1	14.5	10.5	18.1	18.4	3.36	3.85
Total	99.38	99.29	99.71	99.56	99.5	99.3	99.36	99.3	99.64	99.82	99.72
Ba	710	760	640	754	70	1530	1245	30	46	42	38
Cs	0.3	0.5	0.2	0.4	0.3	0.4	0.5	0.8	0.7	0.2	0.3
Cl	5600	6400	4283	7542	2800	54	61	50	57	64	51
Co	1.8	3	2	7	1.8	1.3	2	9.6	8	1	2
Cu	493	264	86	32	436	5	9	12	16	15	11
F	100	141	75	68	70	24	32	41	38	29	23
Ga	16	18	20	15	16	6	75	6	8	1	3
Au	8	6	5	5	6	<5	<5	<5	<5	5	6
Hf	1	3	2	4	1	2	3	3	4	1	4
Mo	35	8	6	3	34	53	32	30	26	14	12
Ni	6	10	7.5	8	6	7	5.4	15	12	6	5
Nb	6	8	5	7	2	6	4	6	8	1	9
Pd	10	6	5	5	5	5	<5	<5	<5	5	5
Pt	12	10	10	10	10	<10	<10	<10	<10	10	12
Rb	5.6	8	6.7	8	6	36	28	9.4	10	3.4	1
Ag	2	4	3	2	2	1	2	2	1	2	3
Sr	430	512	480	410	30	240	312	500	520	430	408
Ta	0.9	1.2	2	1	0.6	0.6	0.5	0.6	0.8	0.6	1.3
Th	2.8	1.2	2	3	0.4	1.4	2	5.2	8	2.8	4
Sn	9	12	4	3	4	18	12	2	5	9	10
W	4	3	2	2	3	76	64	3	4	4	5
V	48	34	29	41	38	59	46	53	49	48	58
Zn	18	14	12	20	18	13	16	130	151	6	8
Zr	40	30	46	52	30	30	46	110	162	40	52
La	18	21	20	19	22	209	228	27.1	28.4	19.4	20
Ce	24.7	26	26.2	25	26.9	271	282	49.9	52	27	29
Pr	2.09	2.2	1.9	2	2.1	22.2	20	5.99	6	2.2	2.4
Nd	5.7	6	5.5	6.4	5.4	62.4	65	21.3	23	5.8	6.8
Sm	1	1.3	0.9	1.2	0.8	6.8	7	4	5	1.4	1.5
Eu	0.16	0.2	0.18	0.21	0.23	2.39	2.6	0.77	0.8	0.24	0.26
Gd	1.08	1.2	1	0.9	1.1	5.19	6	2.56	3	1.2	1.4
Tb	2.8	3	2.6	2.5	3.1	0.79	0.9	0.29	0.34	2.5	2.8
Dy	0.64	0.7	0.6	0.58	0.67	4.47	5	1.57	2	0.8	1
Ho	0.12	0.14	0.1	0.15	0.11	0.83	0.4	0.37	0.4	0.13	0.15
Y	3.3	4	3	4.1	4.4	25.5	28	11.3	14	4.5	5
Er	0.43	0.5	0.4	0.52	0.48	2.45	3	1.06	1.2	0.6	0.7
Tm	0.06	0.07	0.05	0.06	0.05	0.31	0.4	0.18	0.2	0.7	0.8
Yb	0.4	0.46	0.34	0.44	0.4	1.9	2	1.4	1.7	0.5	0.66
Lu	0.07	0.06	0.08	0.09	0.05	0.22	0.3	0.21	0.3	0.1	0.12
Pr/Pr*	1.04	1	0.9	0.94	0.95	0.96	1.04	1.07	1.03	1.08	1.04
Eu/Eu*	0.8	0.8	0.92	1.02	1.19	1.9	1.7	1.13	0.96	0.86	0.86
Gd/Gd*	0.14	0.12	0.12	0.11	0.11	0.78	0.87	1.01	1.09	0.3	0.15
Ce/Ce*	0.9	0.83	0.91	0.9	0.86	0.86	0.85	0.96	0.92	0.9	0.91
Y/Ho	27.5	28.5	30	27.3	27.5	30.72	35.1	30.5	35	34.6	33
La/Yb	45	45.6	58.8	43.18	55	110	98.5	19.35	16.7	38.8	30

malized to chondrite, Post-Archean Australian Shale (PAAS) and North American Shale Composition (NASC), (Fig. 9A, B, C). The patterns display light REE enrichment, subtle to no distinguished Eu and Ce anomaly, (Fig. 10 C, D, E) weak positive Y anomaly and a very prominent positive Tb and Tm anomaly. The most likely explanation for positive signatures of the Tb, Tm and Y and light REE enrichment could be related to the detrital continental inputs from dropstones (Lottermoser and Ahshley, 2000; Baldwin, 2014; Mohseni and Aftabi, 2015) during exhalative subseafloor hydrothermal mineralization. This is also supported by the high ratios of Y/Ho (>27.3, Table 4) and covariation diagrams of Fig. 10A, B, D. The REE + Y enrichment may be related to the

presence of these elements in zircon, xenotime and monazite-rich dropstones.The REE + Y normalized to PAAS and NASC do not display significant variations, though they reflect the reliability and precision of the data.

5.3. Salt rocks and cap carbonates

Major and trace element composition of different colored halite rocks and cap carbonates are shown in Table 4. SiO2 (0.4–6.94%) and Fe2O3 (0.4–3.5%) values are higher than the normal values reported for marine evaporites (Stewart, 1963). This enrichment is probably related to the cryptobandings of jaspilites and salt

Table 4
Major (wt%), minor (ppm), and precious (ppb) elemental contents of halite and cap carbonates.

Elements	Red salt-1	Red salt-2	White salt-1	White salt-2	Grey salt-1	Grey salt-2	Cap carbonates		
							Hormuz-1	Hormuz-2	Mato Grosso
SiO_2	4.5	3.1	0.55	0.4	6.94	5.8	4.3	2.6	0.62
TiO_2	0.04	0.03	0.01	0.02	0.02	0.03	0.03	0.04	0.02
Al_2O_3	0.68	0.61	0.07	0.05	0.65	0.6	0.53	0.6	0.27
Fe_2O_3 (total)	2.94	3.5	0.46	0.4	2.05	2.1	0.56	1.6	0.45
MnO	0.05	0.04	0.01	0.02	0.01	0.02	0.04	0.03	0.18
MgO	0.49	0.63	0.05	0.03	0.06	0.07	22.8	19.65	20.54
CaO	3.46	2.56	0.48	0.5	1.3	2.2	26.5	27.8	31.6
Na	31.2	32.1	34.4	33.6	32.6	31.8	0.7	0.5	–
K	0.22	0.19	0.03	0.03	0.48	0.52	0.3	0.7	0.06
P_2O_5	0.03	0.02	0.02	0.04	0.01	0.02	0.04	0.05	0.03
LOI	13.1	12.5	7.37	8.6	9.7	8.4	43.5	45.86	45.57
Total	99.71	98.88	99.55	99.89	99.62	99.76	99.75	99.43	99.26
Ba	9100	8652	110	132	580	484	86	80	12.32
Cs	0.2	0.1	0.1	0.2	0.1	0.2	0.5	0.2	0.25
Cl	435,000	436,000	565,500	542,000	558,000	526,000	51	54	–
Co	4.2	3	1.1	2	1	2	2	1	1.18
Cu	24	31	5	6	5	8	6	7	11.23
F	340	386	22	24	26	28	20	25	–
Ga	1	2	1	3	1	1	1	1	0.33
Au	<5	<5	<5	<5	<5	<5	<5	<5	–
Hf	2	3	1	1	1	1	1	2	0.15
Mo	4	3	2	3	5	7	2	2	0.91
Ni	9	7	7	6	6	8	5	4	8.86
Nb	1	2	1	1	1	2	1	2	0.38
Pd	<5	<5	<5	<5	<5	<5	<5	<5	–
Pt	<10	<10	<10	<10	<10	<10	<10	<10	–
Rb	5.3	6	0.4	0.6	6.3	5	4	3	1.34
Ag	2	1	2	1	1	2	1	1	–
Sr	350	412	30	43	70	94	48	58	51.02
Ta	0.6	0.8	0.6	0.7	0.5	0.6	0.5	0.7	0.3
Th	0.7	0.9	0.1	0.2	0.6	0.8	0.6	0.5	0.35
Sn	2	3	1	2	2	1	1	1	–
W	2	4	1	3	2	3	1	2	–
V	15	18	7	6	13	16	5	8	6.26
Zn	28	23	13	10	6	8	10	14	207.07
Zr	10	14	1.8	2	13.9	15	14	16	6.38
La	14.9	16	1.3	1.1	12.8	11.6	2	2.6	1.21
Ce	0.2	0.3	1.5	1.2	11.8	12.5	5	6.1	2.48
Pr	1.58	2	0.15	0.2	0.87	0.9	0.4	0.5	0.32
Nd	5	5.8	0.4	0.5	2.3	2.6	2	1.7	1.28
Sm	0.8	0.9	0.1	0.16	0.4	0.46	0.3	0.2	0.27
Eu	0.1	0.12	0.05	0.06	0.09	0.08	0.1	0.09	0.06
Gd	0.68	0.7	0.05	0.07	0.24	0.3	0.4	0.5	0.24
Tb	0.09	0.08	0.05	0.06	0.06	0.07	0.05	0.08	0.04
Dy	0.56	0.6	0.07	0.08	0.19	0.2	0.3	0.24	0.22
Ho	0.09	0.1	0.05	0.05	0.06	0.07	0.08	0.06	0.04
Y	3	3.6	0.5	0.6	1.2	1	3	2.7	0.05
Er	0.36	0.4	0.05	0.06	0.18	0.2	0.3	0.2	0.12
Tm	0.06	0.05	0.05	0.07	0.05	0.06	0.05	0.05	0.02
Yb	0.3	0.37	0.1	0.2	0.2	0.26	0.16	0.3	0.12
Lu	0.05	0.06	0.11	0.15	0.06	0.05	0.06	0.07	0.02
Pr/Pr*	2.5	2.26	0.1	0.15	0.92	0.87	0.75	0.9	–
Eu/Eu*	0.66	0.74	0.74	1.3	1.3	1.01	1.3	1.1	–
Gd/Gd*	1.46	1.4	0.1	0.23	0.65	0.78	1.1	1.16	–
Ce/Ce*	0.009	0.01	0.15	0.6	0.7	0.75	1.3	1.2	–
Y/Ho	33	36	10	12	20	14.3	14.3	45	–
La/Yb	49.6	43.2	13	5.5	64	44.6	12.5	8.7	–

rocks. Barium contents range from 110 to 9100 ppm, indicating the presence of barium sulfate as well as detrital barite. Very high contents of barium up to 1530 ppm have also been reported in diamictite bearing BIFs (Table 4). The concentration of some immobile elements, including Zr (1.8–15 ppm), La (1.1–14.9 ppm), Ce (0.2–12.5 ppm), Nb (1–2 ppm), Hf (1–3 ppm), Ta (0.5–0.8 ppm), Y (0.5–3 ppm) and Th (0.1–0.9 ppm) is 4.5–37.5 magnitudes higher than the marine evaporites (Stewart, 1963). Certainly, these elements do not fulfill the Goldschmidt rules to replace either Na or Cl in halite, thus it is highly likely that they originate from the detrital provenance, probably zircon, xenotime and monazite-bearing dropstone inputs. Houghton (1980) reported that Br values

in Hormuz salts range from 39 to 125 ppm. Compared to the mean content of low-bromide non-marine salts (50 ppm, Tucker, 1991), the bromide concentration in the Hormuz salts may be considered as low bromide groups. These low values may be linked to the low-bromide meteoric water formed by ice melting during Ediacaran interglacial period. The composition of the Hormuz cap carbonates are compared to the famous Neoproterozoic cap carbonates of Mato Grosso, Brazil (Font et al., 2006), (Table 4). Accordingly, CaO, MgO and LOI values are matched with dolomitic limestones. Interestingly enough, the concentrations of immobile elements (Zr, La, Ce, Hf, Nb, Th, Y, Ta, Tb, Tm) in the Hormuz cap carbonates are almost 2–10 times higher than that of the Mato Grosso cap
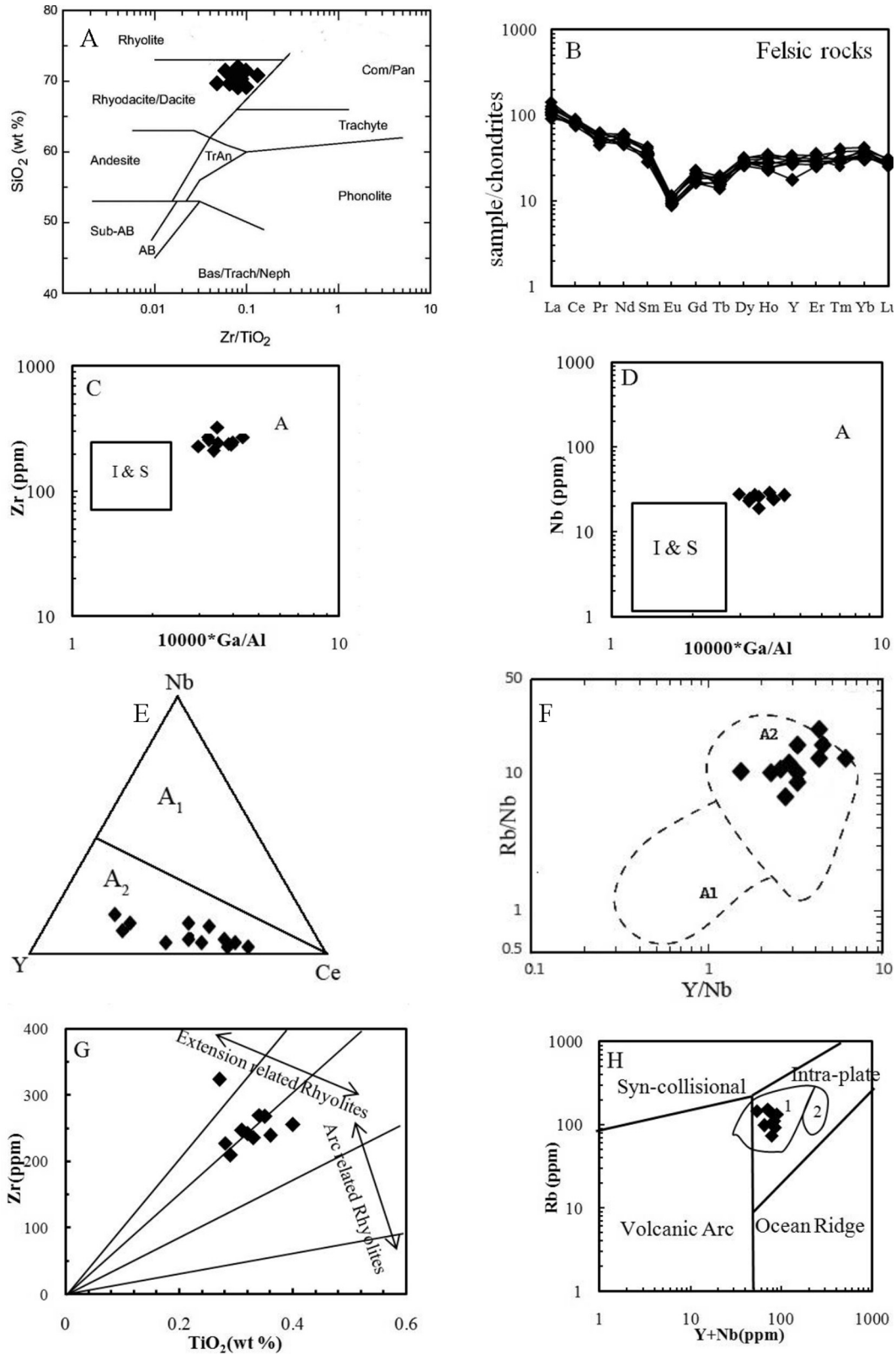
Fig. 8. A. Geochemical position of felsic rocks in SiO₂-Zr/TiO₂ biplot (Winchester and Floyd, 1977). B. Chondrite normalized REE + Y patterns of felsic rocks (Sun and McDonough, 1989). C. Zr-10,000 × Ga/Al diagram (Eby, 1992). D. Nb-10000 × Ga/Al biplot (Eby, 1992). E. Y-Nb-Ce diagram (Eby, 1992). F. Rb/Nb-Y/Nb biplot (Eby, 1992). G. Zr-TiO₂ diagram (Syme, 1998). H. Rb-Y + Nb biplot (Pearce et al., 1984). Numbers in Fig. 8H represent: 1 = Yellowstone Snake River rhyolite, 2 = East African Rift.
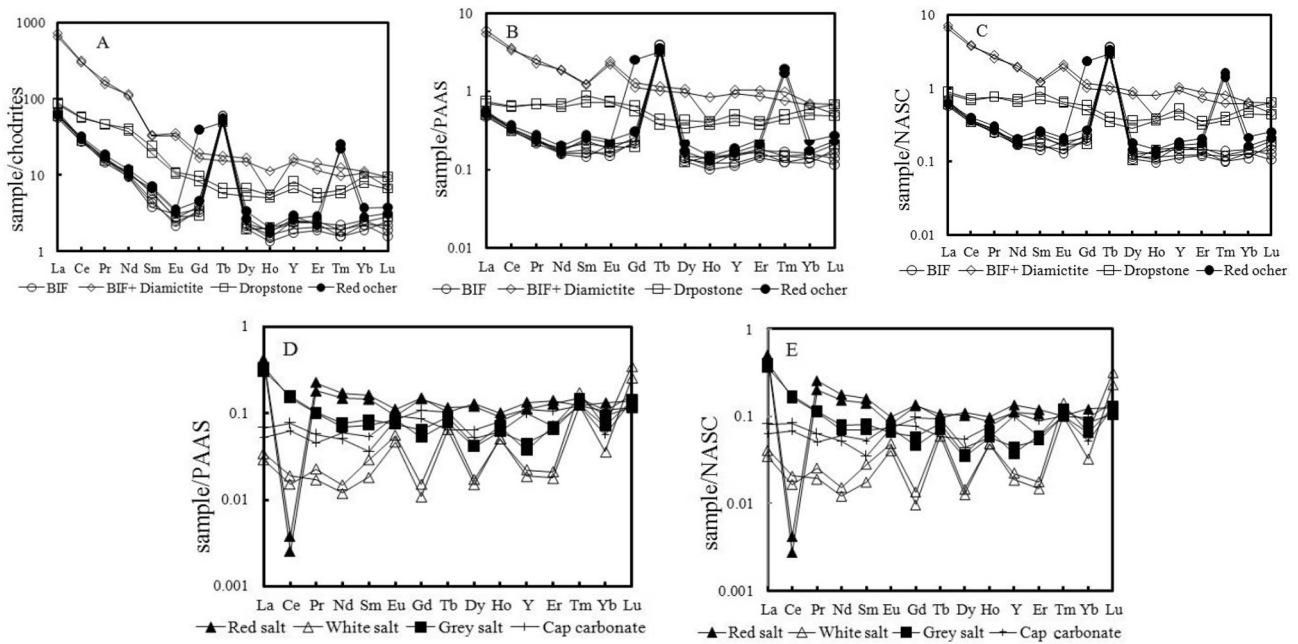
Fig. 9. Rare earth element patterns in banded hematite-chert, salt rocks and cap carbonates. A. Chondrite normalized in banded hematite-chert. B. PAAS normalized in banded hematite-chert. C. NASC normalized in banded hematite-chert. D. PAAS normalized in salt rocks and cap carbonates. E. NASC normalized in salt rocks and cap carbonates.

carbonates. Thus, the high values of immobile elements are related to the detrital-bearing minerals (zircon, xenotime, monazite) in glaciogenic dropstone inputs. Fig. 9D, E indicates normalized patterns of REE + Y of salt rocks and cap carbonates to the PAAS and NASC shale. The patterns display a saw-shape signature, but do not present any significant enrichment (Fig. 9D, E). This may be either related to heterogeneous distribution of the immobile elements within the dropstone-bearing detrital minerals or closeness of the elemental contents to the limit of detection. Cerium gives a distinguished negative anomaly in red salts. This anomaly reflects leaching of the cerium by dissolution and supergene processes of the salts and segregation of Ce to more insoluble Ce^{+4}.

6. Isotopic signatures of the banded iron salt formation

Stable carbon and sulfur isotopes in carbonates, sulfates and pyrite are very useful guides for glacial intervals associated with Neoproterozoic banded iron salt formations. The most distinguished Neoproterozoic glaciations occurred during Cryogenian and Ediacaran time. Cryogenian glaciations timeline include Sturtian galciation period (750–710 Ma) and Marinoan glaciation periods (650–636 Ma). Ediacaran glaciation timelines cover Sinian glaciations period (635–580 Ma) and Gaskiers glaciations period (570–541 Ma) (Halverson et al., 2010). Houghton (1980) and Ghazban and Al-Aasm (2010) performed valuable isotopic data at Hormuz Island. Ghazban and Al-Aasm (2010) determined the carbon isotopic composition of black dolomites, which are similar to those of the black cap carbonates of cherty-shaley dolomitic composition. These carbonates show considerable depletion in $\delta^{13}C$, with a range from −0.8 to −2.07 per mil VPDB (Ghazban and Al-Aasm, 2010). The values also correlate with one of the important negative excursion in the $\delta^{13}C$ carbonate curve developed by Derry et al. (1992). The presence of Collenia in black cap carbonates together with U-Pb dating (558 ± 7; Faramarzi et al., 2015) in zircon, and the negative $\delta^{13}C$ excursion probably correlate with the post-Gaskiers or Late Ediacaran glacial intervals. Similar evidences of 560 Ma Ediacaran glaciation have been reported by Etemad-

Saeed et al. (2015) in northern Iran. Globally, this excursion correlates with $\delta^{13}C$ values of cap carbonates in Buah (Huqf Supergroup Formation), Oman that belongs to about 554 Ma (Fike et al., 2006; Fig. 1).

The $\delta^{18}O$ in cap carbonates ranges from 15.24 to 17.90 per mil VSMO or −15.33 to −12.61 per mil VPDB. The values plot within the hydrothermal field of carbonates described by Allan and Wiggins (1993). By plotting these values on the diagram of Loyd et al. (2015; Fig. 4), the temperature of cap carbonate formation is about 200 to 280 °C. This range of temperature is consistent to 215 °C (Ghazban and Al-Aasm, 2010), obtained by fluid inclusions in dolomite and within the range of 40–370 °C reported by Loyd et al. (2015). This range of temperature for cap carbonates points to the continuous effect of geothermal system during the final stage of synchronous felsic volcanism and associated exhalative hydrothermal banded iron salt formation. In this regard, Ghazban and Al-Aasm (2010) suggested that the high temperature of precipitation for dolomitic carbonates at Hormuz Island could be related to the seawater–rock interaction.

The negative $\delta^{13}C$ excursion in cap carbonates is also supported by an average of 28 per mil $\delta^{34}S$ for terminal Neoproterozoic-Lower Cambrian (Houghton, 1980) time and correlates with Late Ediacaran.

7. Discussion

In order to explore the genetic aspects of BISF at Hormuz Island, the geological features, previous alternative models and the refined model of Ediacaran BISF are discussed:

7.1. Geostructural anatomy of Hormuz Complex

The Ediacaran Hormuz complex is characterized by synchronous felsic volcanism and glaciogenic dropstone-bearing banded iron salt formation, probably formed in rift-related shallow composite graben-like basins in Proto-Tethyan ocean of the Gondwana during the Pan-African orogen. This tectonic setting is in
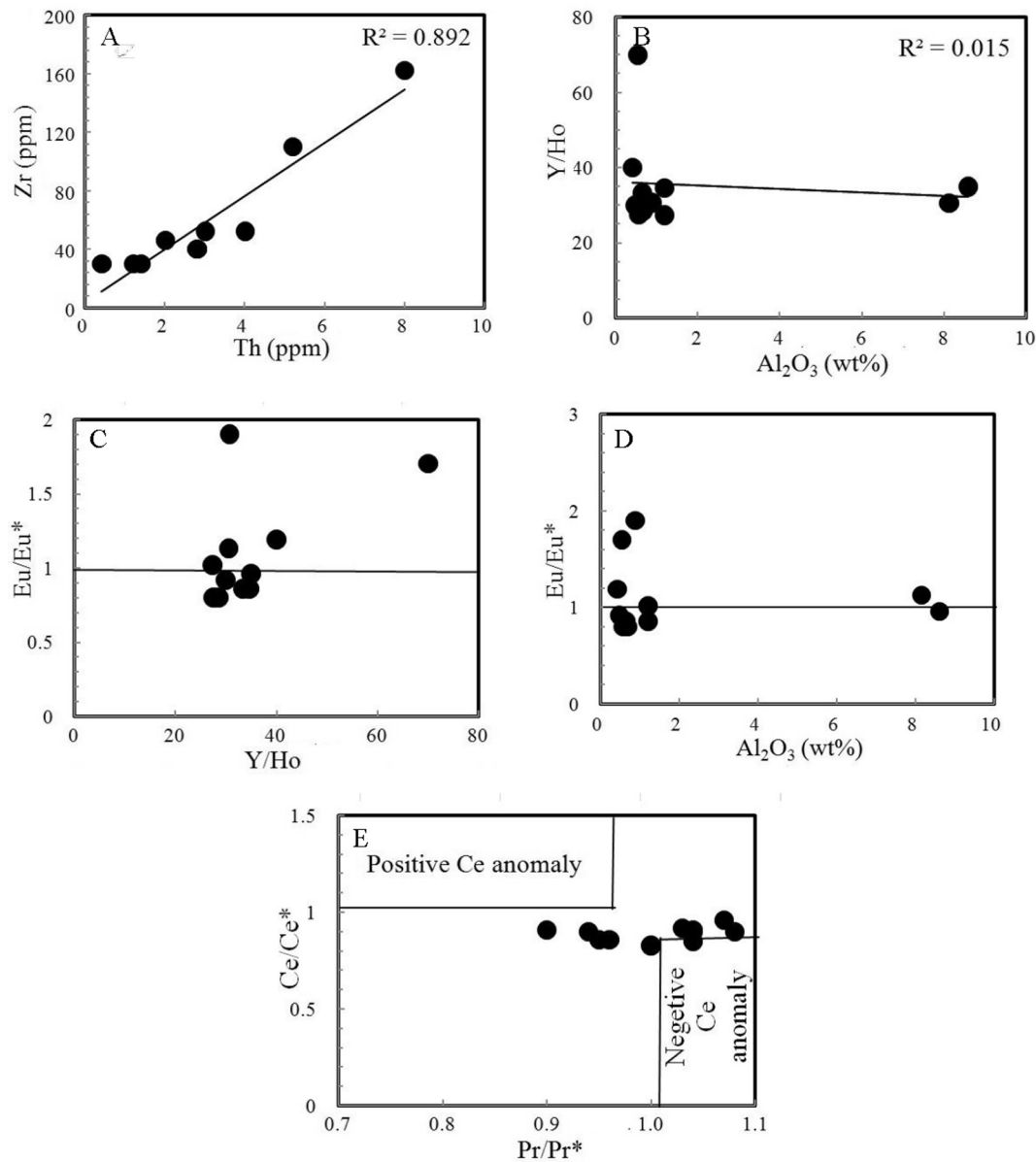
Fig. 10. Covariation biplots in banded hematite-chert. A. Zr-Th. B. Y/Ho-Al$_2$O$_3$. C. Eu/Eu*-Y/Ho. D. Eu/Eu*-Al$_2$O$_3$. E. Ce/Ce*-Pr/Pr*.

accord with petrogeochemical and tectonomagmatic signatures of rift-related A-type rhyolitic volcanism. Felsic rhyolitic volcanism and associated banded iron salt formation occur as proximal pyroclastic tuff cone and distal banded jaspilitic and salt rocks. The proximal facies is composed of fine to coarse-grained chloritized, actinolitized and tourmalinized hyaloclastites that are linked to massive hematite-rich mineralization. The distal facies is associated with extensive tuffaceous banded jaspilitic-hematitic and salt rocks, though the only unique feature is the unusual association of banded jaspilite-salt formation.

7.2. Structural and textural signatures of the glaciogenic banded iron salt formation

There is not much recorded data on the structural and textural relations of the Ediacaran-type banded iron salt formation, except the Ediacaran BIFs in Bafq iron mining district in Iran (Mohseni and Aftabi, 2015). Heidarian et al. (2017) proposed that the iron ores in the Bafq mining district are of IOCG–Kiruna type as well as representing jaspilitic iron deposits. The occurrence of jaspilites is the most distinguished sign of BIFs rather than IOCG-Kiruna type model of iron mineralization. Unfortunately, the authors were not able to observe the frequent association of jaspilites, glaciogenic boulders and dropstones (Mohseni and Aftabi, 2015, p. 219–221) with BIFs in the Chadermalu area. Additionally, the low contents of copper and gold in ore and low salinities (0.3–24 wt %) in apatites (compared to 10–50 wt% in IOCG-Kiruna ores, Bekker et al., 2014), rule out the Kiruna-type model of iron mineralization at Chadermalu iron mine.

The banded iron salt formation at the Hormuz Complex shows typical macrobanding, mesobanding, microbanding and probably cryptobanding layers between jaspilitic hematite, anhydrite and halite (Figs. 4 and 5). The jaspilitic and hematitic bands consist of finely recrystallized chert and hematite, probably formed as silica (H$_4$SiO$_4$) and ferrihydrite or Fe (OH)$_3$ gels during syndiagenetic stage. Macrobandings mainly occur in the proximal flank of the pyroclastic tuff cone and contain very minor amounts of salt minerals. The mesobandings and microbandings are mostly developed

in the distal depositional facies around the pyroclastic tuff cone. The presence of fine layering in tuffaceous hematite and salt minerals may indicate that they were deposited under quiet depositional basins. The alternating bands of hematite and salt minerals are not consistent with the normal evaporation sequence of evaporites (Krauskopf, 1967). In the normal sequence of evaporites (Krauskopf, 1967), hematite precipitates before or along with calcite without precipitating sequentially with anhydrite or halite. This is related to the lower solubility of hematite compared to calcite or salt minerals. As such, the cyclic bandings in hematite and salt minerals are probably related to synchronous seawater evaporation associated with exhalative hydrothermal pulses of mineralizing solutions and successive periods of submarine felsic volcanism. This is supported by the association of hematite, halite and anhydrite with apatite, tourmaline and chlorite. An exceptional feature of the banded hematite-salt rocks is the presence of bullet-shape dropstones, which have not yet been reported in the evaporites. This indicates that seawater evaporation was synchronously active during glaciomarine deposition of iron oxide-salt minerals. Moreover, Houghton (1980; p. 23), reported the occurrence of specular hematite at grain boundaries and as inclusions in halite crystals, which may point to the hydrothermal origin of both halite and hematite. This is supported by the homogenization temperature (213–216 °C) of the halite-liquid-vapor phase of fluid inclusions in dolomite crystals (Ghazban and Al-Aasm, 2010).

One of the significant structural features in the banded iron salt formation of the Hormuz Complex is the presence of exotic glacial clasts or dropstones, which have no petrological provenance with the substrates of rhyodacitic-rhyolitic tuffs, hematite and salt minerals. Few of the clasts are angular, but most of them are subrounded-rounded. Some of the fragments deflect the laminae below sediments, but the overlaying sediments drape the clasts (Fig. 6E). The clasts are composed of cherty marble, epidotized clasts, metamudstone and some are also polygenetic. The lack of striated clasts and frequent occurrence of the polygenetic dropstones indicate that the depositional environment was of subaqueous glaciogenic. The subrounded-rounded nature of the dropstones may indicate that they were derived from the melting of glacial streams, originated by the continental glaciers or moranes. Despite the clear and great relevance of glaciogenic dropstones, in particular planar and bullet–shape dropstones (Fig. 5), Smith (2012), interpreted the clasts as the exotic blocks of metamorphosed limestone, metamorphosed mudstone, schist and gneissic granite. Smith (2012) also assumed that the exotic clasts to have been originated from the Pan-African metamorphic basement fault scarps in the salt domes of Persian Gulf. Since the exotic or xenolithic clasts do not show any evidence of compact breccias, flow structure and mylonitic texture, thus they could not have been originated from the fault scarps. In this regard, Ali et al. (2010) and Stern et al. (2006) reported similar diamictites and dropstones in the Arabian-Nibian shield.

Regarding the glaciogenic or non-glaciogenic nature of the dropstones, Pettijohn (1975), suggested a modal content of less than 10% pebbles – cobbles for the glaciogenic dropstones. In contrast, volcanogenic clasts (airborne pyroclastics, ejecta and lahars) and debris flows contribute to more than 50% of the homogeneous volcanic origin or sedimentary clasts (Waitt, 2013; Goudie, 2004). The dropstones in the BISF of the Hormuz Island contain about less than 8% of pebble or cobble size and their composition is close to those of silicious marble or calc-silicate marble (Table 3), thus they show no affinity to the volcanogenic rhyolitic clasts or debris flows. It is noteworthy that the clasts were previously recognized to be of metamorphic rocks (Player, 1969; Kent, 1979; Smith, 2012), but their origin was enigmatic. As there is no exposed metamorphic basement in the Hormuz Island, the clasts should have come from

distant sources, probably the metamorphic Arabian-Nubian shield during the Ediacaran glacial timelines. No significant fault displacements or stratigraphic truncations have been observed in the geological units, but the clasts deflect the jaspilitic layers (Figs. 5D and 6E), implying that they formed during early diagenetic stage.

The isotopic signatures and the presence of genus Collenia in the Hormuz Complex together with the possible recognized glaciation timelines in the Late Ediacaran (Hebert et al., 2010; Vernhet et al., 2012) attest to the possible glaciogenic origin of the dropstones in BISF. However, due to the lack of zircon age data on the dropstones, the exact age and provenance of the dropstones are unclear and they merit further radiogenic and stable isotopic studies.

7.3. Geochemical signatures of glaciogenic Ediacaran banded iron salt formation

There are several glaciation timelines during Neoproterozoic, including Sturtian, Marionan and Gaskiers, which are linked to synchronous basic to felsic volcanism. The most recognized glaciogenic BIFs include Rapitan-type (Canada), Jakkalsberg (southern Namibia), Chuos Formation (northern Namibia) and Jacadigo (southwestern Brazil) (Gaucher et al., 2015). There are no significant differences between most of the major element components of the Hormuz BISF and those of the Algoma, Superior and Rapitan-type BIFs worldwide. However, the only exception is attributed to the highest values of Na_2O (1.2%), chlorine (7542 ppm) and K_2O (0.9%). This is probably linked to the presence of salt cryptobandings within the banded jaspilitic hematite. High concentrations of Zr (30–162) ppm, Ba (70–1530 ppm), Hf (1–4 ppm), Nb (2–9 ppm), Ta (0.5–2 ppm), Th (0.4–8 ppm), La (18–228 ppm), Ce (24.7–282 ppm) and Y (3–25.5 ppm) in banded iron salt formation, dropstones and diamictites, reflect a detrital origin, probably provided by the glaciogenic dropstones. The contents of immobile elements (Zr, Ta, Th, Hf, Nb, La, Ce, Y) in salt minerals of the Hormuz BISF are 2–10 magnitudes higher than the normal content of the marine evaporites (Stewart, 1963). This is interesting as these elements could not replace the structure of halite, thus they certainly have a detrital origin from the glaciogenic dropstones rather than by normal seawater evaporation.

The geochemistry of cap carbonates has been considered as a criterion for glaciogenic environments (Font et al., 2006; Gaucher et al., 2015; Mohseni and Aftabi, 2015). In this regard, Zr, Hf, Nb, Ta, Th, La, Ce and Y contents in the Hormuz cap carbonates are almost two times higher than the cap carbonates of the Mato Grosso at Brazil. The high values are possibly related to the presence of detrital zircon, monazite and xenotime carried by dropstones from the continental glaciers or moraines. The absence of jaspilitic hematite and salt rocks in cap carbonates indicate that the airborne pyroclastics were diminished during the cap carbonates formation, though a weak hydrothermal system may have been active. As such, the high values of the immobile elements were not the result of airborne pyroclastics, but were possibly derived from the glaciogenic dropstones during interglacial time.

The geochemical signatures of REE + Y in banded iron salt formation of the Hormuz Complex display light REE enrichment, a very strong Tb–Tm anomaly, a weak positive Y anomaly, but no distinguished Eu or Ce anomalies. These signatures are caused by the presence of detrital continental inputs from dropstones. Lottermoser and Ahshley (2000), Baldwin et al. (2012) and Mohseni and Aftabi (2015) also suggested similar REE + Y patterns for glaciogenic BIFs. The lack of distinguished reduced Eu anomaly may have caused dilution of the hydrothermal inputs by the oxidizing oceanic water during Neoproterozoic, which also have been reported by Klein and Beukes (1993) for glaciogenic BIFs. The REE

+ Y patterns in salt rocks and cap carbonates do not give significant variations, except for La enrichment and a negative Ce anomaly. The negative Ce anomaly is due to the oxidation of hematite-rich salt minerals.

7.4. Carbon, oxygen and sulfur isotopic variations in Hormuz BISF and global Ediacaran glaciogenic deposits

Glaciogenic cap carbonates of Ediacaran time display a distinguished negative $\delta^{13}C$ excursion (Derry et al., 1992). The cap carbonates at Hormuz Complex reflect a marked negative depletion in $\delta^{13}C$, (−0.81 to −2.07 per mil) (Ghazban and Al-Aasm, 2010). Similar negative $\delta^{13}C$ excursion in the Ediacaran glaciogenic microbial carbonates and cap carbonates in northern Iran and Bafq iron mining district were reported to be −5.4 to −1 per mil (Etemad-Saeed et al., 2015) and −6.6 to −0.4 per mil (Mohseni and Aftabi, 2015), respectively. These variations are close to one of the distinguished negative excursions in the $\delta^{13}C$ carbonates in the Ediacaran time described by Derry et al. (1992; Fig. 16) and illustrated in Fig. 11 of this study. Importantly, the $\delta^{13}C$ values may show the possible additional Late Ediacaran glaciation record (Fig. 11), supporting the view of multiple Ediacaran Period glaciations proposed by Hebert et al. (2010) and Vernhet et al. (2012). Also, the values are close to the negative excursion of the Ediacaran of Buah cap carbonates, Huqf Supergroups, Oman (Fike et al. (2006; Fig. 1). One of the best distinguished sign of global Ediacaran glaciation is also related to the occurrence of phosphorous-rich banded iron formation (Ilyin, 2009), which is indicated by the presence of apatite-rich hematite at the Hormuz Complex (Fig. 5A).

Based on the average sulfur isotopic studies of sulfates (+28 and range of +21 to +33 per mil) presented by Houghton (1980), in anhydrites and associated banded iron salt formation, the Hormuz Complex have been considered to be of Neoproterozoic-Lower Cambrian time. These values are in agreement with the sulfur isotopic data (Fike et al., 2006; Fig. 1; Fike and Grotzinger, 2008; Fig. 1) of the Buah, Huqf Supergroup of Oman evaporites, although Strauss (1993) suggested that the highly sulfur isotopic values correlate with Ediacaran timeline. This is also supported by plotting the average sulfur isotopic data (+28 per mil) on Fig. 1 of Fike and Grotzinger (2008), which approximately plots within the Late Ediacaran time.

7.5. A refined model of Ediacaran glaciogenic banded iron salt mineralization

7.5.1. Previously proposed model of iron and salt mineralization
Previous studies have given much attention to the geological aspects of the Hormuz Island, but did not explore the genetic aspects of banded iron salt mineralization. In this regard, some of the valuable views on the iron-salt mineralization are described as below.

7.5.2. Magmatic mineralization
Walther (1968) and Kent (1979) reported that widespread hematite mineralization in the Hormuz salt plug to be of magmatic origin as well as syngenetic rather than hydrothermal. The widespread association of banded jaspilitic hematite with salt rocks is inconsistent with the magmatic model of mineralization, although
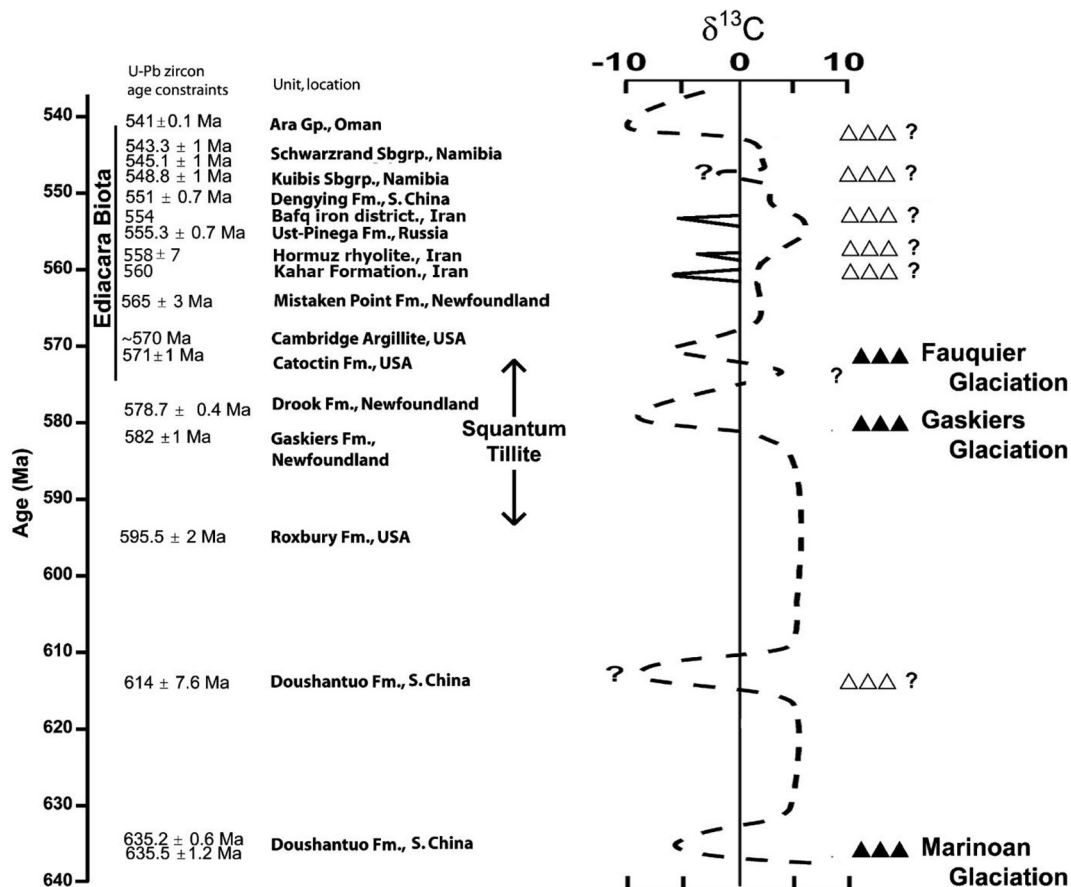

Fig. 11. Marinoan-Ediacaran isotope stratigraphy and possible Ediacaran glacial timelines (modified from Hebert et al., 2010). Iranian isotopic data from: Ramazani and Tucker (2003), Ghazban and Al-Aasm (2010), Mohseni and Aftabi (2015), Etemad-Saeed et al. (2015) and Faramarzi et al. (2015). Filled triangles represent known glacial timelines and open triangles indicate the possible glacial timelines, including the Iranian ones.

Kent (1979) approved of the syngenetic type of iron-salt mineralization.

7.5.3. Shallow marine sabkha-type evaporites

Ala (1974) proposed a shallow marine, intertidal to supratidal, model for evaporite deposition for the Hormuz salt rocks, but did not comment on the exact model of iron mineralization. Isotopic studies by Houghton (1980) and Ghazban and Al-Aasm (2010) indicated a shallow marine evaporite model for salt rocks of the Late Proterozoic-Early Cambrian time. However, fluid inclusion investigations by Ghazban and Al-Aasm (2010) suggested that the homogenization temperature of liquid-gas-halite phase in dolomite ranged from 213 to 216 °C. This indicates a synchronous hydrothermal activity during dolomite and halite deposition. Bosak et al. (1998) studied the regional aspects of the salt plugs in the Persian Gulf, but did not discuss the genetic aspects of iron and salt formation. Talbot et al. (2009) proposed a playa-sabkah as well as marine evaporite model for hematite and salt rocks, but did not suggest any specific model for hematite-salts mineralization. Warren (2006, 2012) gives a comprehensive report on the world evaporites, but no information was given on the genesis of banded iron and salt mineralization.

7.5.4. Ferruginous magmatic-agglomeratic model of mineralization

Faramarzi et al. (2015) suggested that the Hormuz rhyolites and evaporites were synchronously formed at about 558 ± 7 Ma in an extensional backarc, rift-related basins, calc-alkaline or shoshonitic hotspot volcanism, mantle-related Hadean felsic rocks (not described by Faramarzi et al., 2015 on the Ti diagram of zircons), evolving rift (not shown by Faramarzi et al., 2015 on the trace element diagrams of zircons), continental arc and subduction-related arc setting. However, the authors considered the banded iron salt mineralization as the Fe-Mn ferruginous agglomerates. This is highly unlikely, as the agglomerates are the products of strombolian alkaline to peralkaline basaltic eruptions and could not be linked to the rhyolitic volcanism (Atapour and Aftabi, 2017). Geotectonically, BIFs are reported to form in intracratonic island arc (Algoma), rift-drift stage (Superior) and rift–related setting (Neoproterozoic glaciogenic BIFs) (Force et al., 1991; Hagemann et al., 2016). Therefore, the formation of the Hormuz rhyolites and BISF in a continental arc setting (Faramarzi et al., 2015) is highly debatable, in particular for the occurrence of hotspot-type rhyolites. This is also inconsistent with the salt deposits formed in rift-related setting of the alkaline volcanism (Momenzadeh, 2007), although the reported cases of salts and BIFs in a continental arc setting are yet unknown.

7.5.5. Kiruna-type iron ores

Daliran (2002) considered that the hematite-apatite mineralization at Hormuz Island is similar to Kiruna-type at Bafq region. However, the most frequent iron mineral in Kiruna-type ores is brecciated-vein type magnetite, which is different from the jaspilitic hematite at the Hormuz Island. As such, the occurrence of jaspilitic hematitic-apatite ore association at Hormuz Island is better correlated with BIFs rather than magnetite-rich Kiruna ores. Furthermore, the host rock associations in Kiruna-type ores are linked to the alkali granites and carbonatites (Williams et al., 2005), whereas the main host rock to the jaspilitic hematitic at Hormuz Island is A-type rhyolite (Atapour and Aftabi, 2017). It should be noted that none of the above-mentioned models described the glaciogenic structures and jaspilitic nature of the iron-salt mineralization.

The presence of synchronous proximal submarine felsic volcanism, distal dropstone-bearing banded iron salt formation and high to low temperature alteration assemblages provides insight into the existence of the subseafloor hydrothermal system for BISF at the Hormuz Island. A possible four-stage genetic model is illustrated as below (Fig. 12A, B, C, D):

7.5.6. Stage 1: Rift-related submarine felsic volcanism, followed by the glacial ice sheet formation

According to Fig. 12A, the first stage of BISF model begins with submarine rifting, felsic eruptions of rhyolite-rhyodacite, ice sheet formation due to the sulfur dioxide rich volcanic gases, interaction of seawater with felsic magma, and generation of subseafloor hydrothermal fluids. In this regard, Young (2002) proposed that most of the Neoproterozoic glaciogenic BIFs were formed by subseafloor hydrothermal activity in rift-related settings. It is widely known that felsic magmatic eruptions are rich in sulfur dioxide and may produce cooler climate conditions for glacial periods and snowbnall earth conditions (Self, 2006). One of the key evidence of the Ediacaran snow ball earth is the presence of banded hematite associated with dropstones (Young, 2002; Shields, 2005). This is well supported by widespread synchronous felsic volcanism and associated glacial activity during Cryogenian and Ediacaran, rather than non-volcanic Tonian time of the Neoproterozoic (Stern et al., 2008; Mohseni and Aftabi, 2015). The volcanogenic SO_2 fluxed into the atmosphere, ocean and produced sulfuric acid, thereby decreasing the pH of the ocean to acidic ranges. The acid production is very fast, as the residence time of SO_2 in the atmosphere and ocean is about 40 days (Mason and Moore, 1982). By continuous rifting activity and submarine felsic volcanism, the seawater is drawn into the subseafloor and gets hotter as it reacts with felsic magma (Fig. 12A). The H_2SO_4-rich heated seawater reacts with rhyolitic rocks and sediments, releases H_4SiO_4 by hydrothermal hydrolysis and dissociates seawater to $H_2O = H^+ + OH^-$. This is followed by the reaction of Mg^{+2} of the seawater with H_4SiO_4, which forms chlorite and other Mg-rich hydrous-altered silicate minerals. The reaction increases the activity of H^+ and produces an acidic hydrothermal solution with pH range of 1–4 (Seyfried and Bischoff, 1977; Hajash and Chandler, 1981).

Experimental investigation at 200–500 °C and 1000 bars (Hajash and Chandler, 1981) on the interaction of seawater with rhyolite produces hydrous Mg-silicate minerals (chlorite, albite, actinolite, epidote and anhydrite) and exhalative hydrothermal fluids that contain high contents of Fe, Si, P and other elements (Seyfried and Bischoff, 1977; Hajash and Chandler, 1981).

The reaction of seawater with felsic magma and sediments produced Mg-rich hydrous alteration minerals, but leached considerable amounts of Si, Fe, P to form exhalative hydrothermal fluid. This is supported by high MgO and Fe_2O_3 and LOI values in altered rhyolites at the Hormuz Island. The ice sheet formation is known as "Snowball Earth" during glacial periods, by which the entire surface of the earth was repeatedly plunged into freezing conditions (Hoffman et al., 1998; Holland, 2005; Young, 2002; Shields; Hoffman et al., 2011). The ice formation provides a highly reducing condition to the ocean, which results in accumulations of more ferrous iron in solution and in deeper parts of the ocean (Holland, 2005).

Hajash and Chandler (1981) found that significant percentage (21%) of Fe was leached during the seawater interaction with rhyolitic rocks, much higher than any other igneous rocks. This indicates that in submarine felsic volcanism significant amounts of iron and other elements are released from rhyolitic rocks into the hydrothermal fluids, a case which made the ground preparation for the formation of hydrothermal BIFs at the Hormuz Complex.

7.5.7. Stage 2: Interglacial period, ice melting, alteration and banded iron salt formation

In contrast to sulfur dioxide diffusion during felsic submarine volcanism, other gases including water and carbon dioxide were
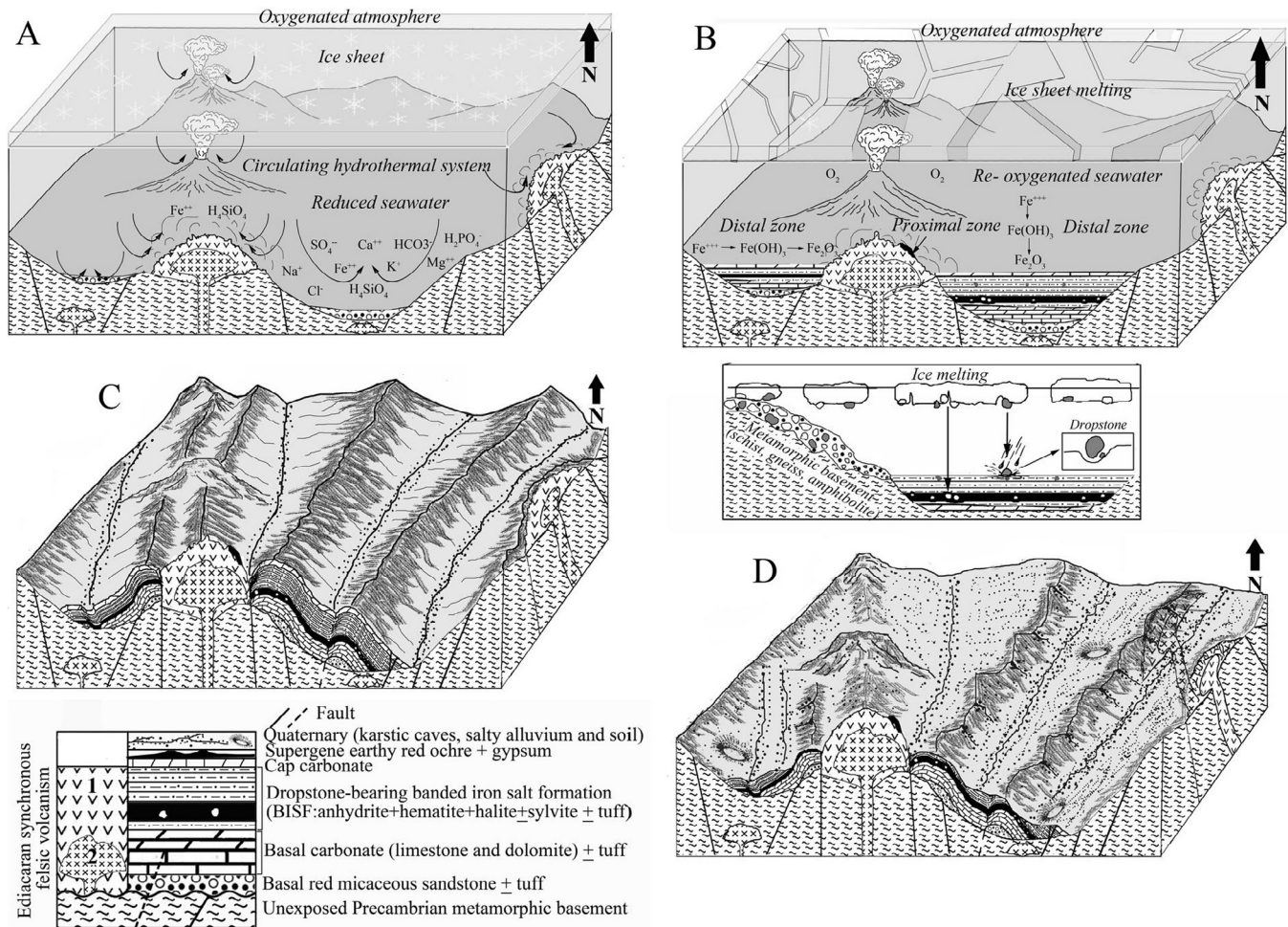
Fig. 12. A possible schematic reconstruction model for the Hormuz BISF in shallow-rifted basins (not to scale). A. Rift-related submarine felsic volcanism, followed by ice sheet formation during glacial period. B. Ice sheet melting, episodic oxygenation and synglaciodiagenetic BISF during interglacial period. C. Tectonism, folding and faulting. D. Residual supergene mineralization and karstification. The numbers in stratigraphic column of felsic volcanism represent: 1 = pyroclastic tuff cone, 2 = cryptodome.

also released into the atmosphere and ocean. However, carbon dioxide in particular has been reported to have a longer timescale warming effects. This led to the warming and ice sheet melting during the interglacial periods (Self, 2006; Stern et al., 2008; Mohseni and Aftabi, 2015). This is also related to the longer residence time of CO_2 (30 years), compared to SO_2 (40 days) in the atmosphere and ocean (Mason and Moore, 1982). As shown in Fig. 12B, during the interglacial periods, the ice sheet is melted and the ocean would come into contact with the oxygenated atmosphere, thus accelerating the diffusion of dissolved oxygen into the ocean.

Shields (2005) explained that the formation of banded hematite formation was due to the episodic waxing and waning of the ice sheet. This is consistent with the cyclic bands of jaspilitic hematite and salt minerals due to the repeated oxidation of ferrous iron, followed by periodic increasing or decreasing strength of the ice sheet. Experimental studies on salt precipitation shows that solid salt or halite precipitates in the supercritical seawater above 430 °C (Hovland et al., 2006). This temperature is in accord with the experimental results of Hajash and Chandler (1981) and alteration assemblages (hematite, apatite, actinolite, sericite, tourmaline, chlorite, albite and anhydrite) in the Hormuz Complex. Hematite, albite, amorphous silica and anhydrite are reported to form during the interaction of seawater with rhyolite at 200–500 °C (Hajash and Chandler, 1981). Furthermore, the association

of hematite, apatite, actinolite, tourmaline, chlorite and albite in banded iron formations has been reported to occur at 200–400 °C (Slack, 1993; Thompson and Thompson, 1996). This range of temperature overlaps the 117–564 °C obtained by fluid inclusion and Raman spectroscopy on the apatites of the Hormuz Complex (Padyar et al., 2012). Seawater becomes supersaturated with anhydrite beyond 130 °C to 500 °C (Seyfried and Bischoff, 1977; Hajash and Chandler, 1981). In this regard, the presence of anhydrite in both distal and proximal ore zones at the Hormuz Complex indicates that the temperature of hydrothermal alteration and banded iron salt formation has been within the range of 130–500 °C. The exact mechanism by which the alternating bands of hematite, chert and salt minerals formed is yet unknown. However, the interaction of high-low temperature upwelling hydrothermal fluids and diffusion of oxygenated seawater are the main factors for syngenetic deposition of banded iron salt formation, though episodic oxygenation, evaporation and solubility of different salt minerals are the other contributing factors.

Episodic oxygenation is the main factor for hematite bandings. This is assumed to result from the cyclic reaction of dissolved oxygen with ferrous and ferric iron provided by ice melting during the warm climate in the interglacial period (Burns, 1993). The final products of the reaction include ferrihydrite, goethite and finally hematite during syngenetic mineralization. Experimental studies (Smith and Lidd, 1949; Burns, 1993) show that goethite transfor-

mation to hematite could occur between 125 and 165 °C. The presence of dropstones in hematite bandings implies that the syngenetic mineralization was synchronously associated with glaciomarine deposition. The lack of distinguished Eu and Ce anomalies in banded hematite layers may suggest that the hydrothermal fluids were diluted by ocean water, but enriched by ice melted water as well as continentally derived dropstone inputs.

It is well accepted that colloidal silica is more soluble up to 900 ppm in thermal waters of present-day geothermal system (Barnes, 1979). This may indicate that high temperature evaporation from the ocean could have caused silica oversaturation and precipitation of silica gel, which during diagenesis transformed to chert bandings, although precipitation may be caused by changes in pH and electrolyte concentration of Na^+ (Barnes, 1979). Since the banded hematite-chert layers are depleted in aluminum, Fe and Si appear to have been originated from the hydrothermal fluids. This is also shown in Fig. 13A, B, C, on which the composition of the Hormuz banded iron salt formation plots within the hydrothermal fields of Ediacaran banded iron formation.

The normal marine evaporite mineral sequences start with the least soluble salts and finish with the most soluble ones. The first products of evaporation are calcite and dolomite, which form when 47% of the seawater is evaporated. Calcite and dolomite in the form of carbonate rocks make the basal sequence of the banded iron salt formation at the Hormuz Complex. As evaporation continues and the salinity reaches to about four magnitudes to that of the original seawater, gypsum and anhydrite are precipitated (Tucker, 1991; Warren, 2012). At about 90% of the seawater evaporation, halite is precipitated and in the final stage of evaporation, sylvite and Mg-salts crystallize. In contrast to the normal sequence of evaporation, there are several cycles of mineral precipitation-mineralization at Hormuz Island, including anhydrite-hematite followed by halite-hematite and so forth. This shows that the evaporation and precipitation of banded iron-salt rocks were mainly controlled by repeated submarine volcanism, cyclic inputs of exhalative hydrothermal fluids and episodic oxygenation during the interglacial period. The frequent association of primary anhydrite with banded hematite and hydrothermal alteration assemblages may suggest that anhydrite is of hydrothermal origin. This
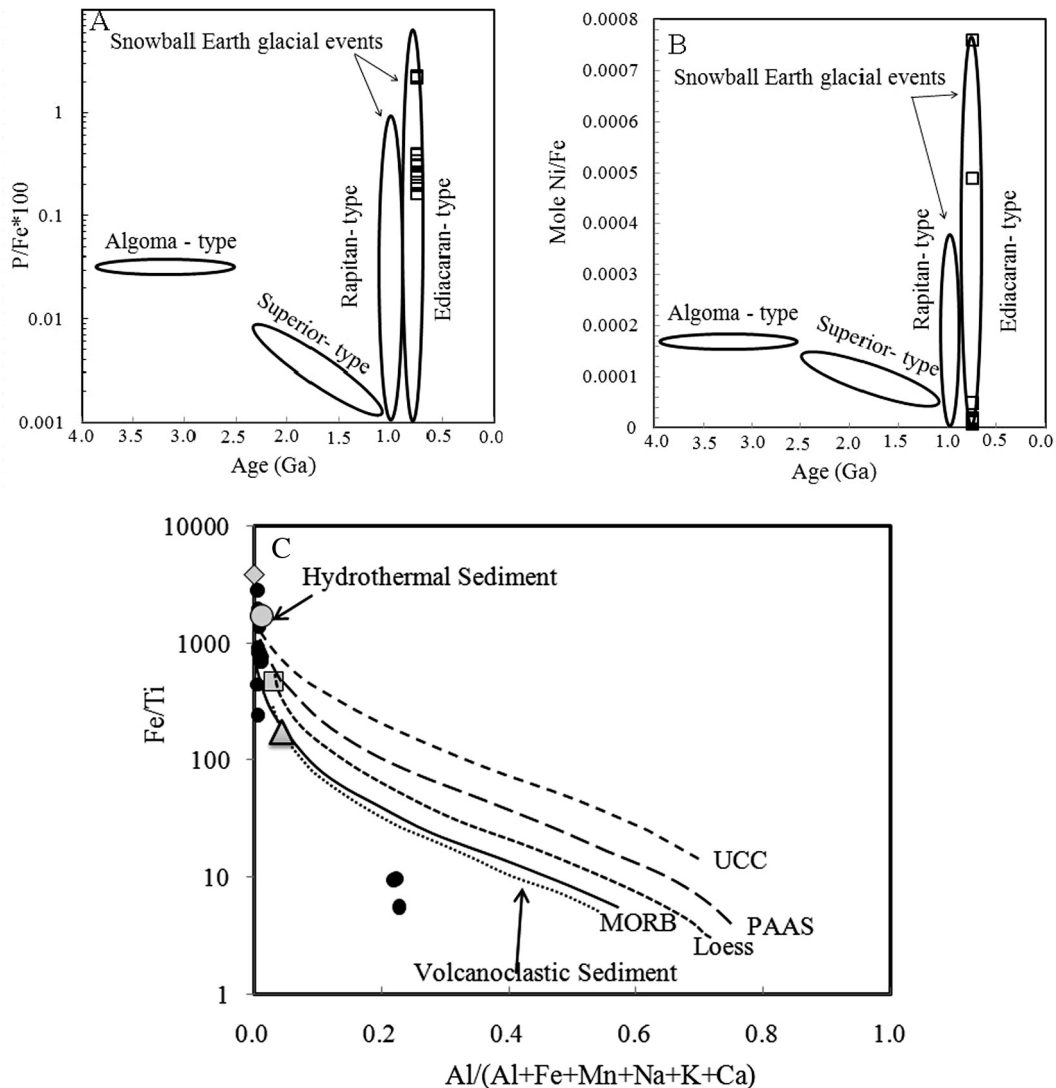

Fig. 13. Discrimination diagrams for different types of banded iron formations. A. P/Fe × 100-Age (Ga) (Bekker et al., 2014). B. Mole Ni/Fe-Age (Ga) (Pecoits et al., 2009; Bekker et al., 2014). C. Fe/Ti versus Al + Fe + Mn + Na + K + Ca (Cox et al., 2013) for Algoma (triangle), Superior (square), hydrothermal sediments (open circle), Rapitan (diamond), Hormuz BISF (filled circle), composite shale (PAAS) and upper continental crust (UCC).
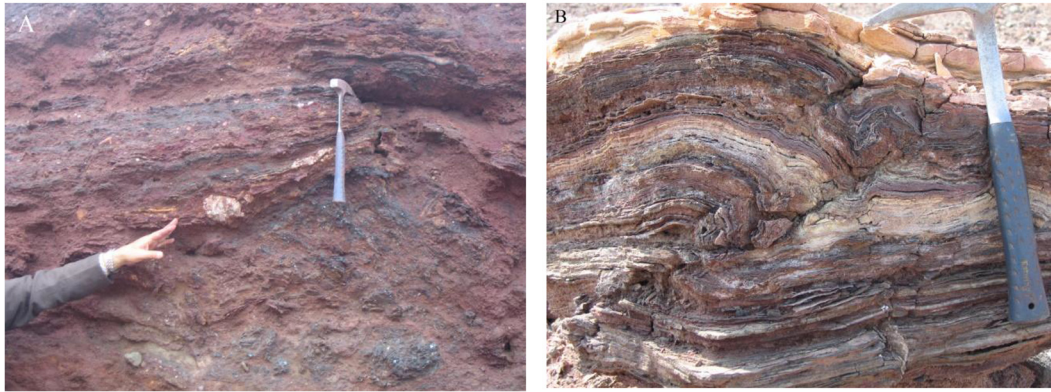
Fig. 14. A. Faulting. B. Faulted drag folding in banded iron salt formation.

is consistent with the experimental findings of Hajash and Chandler (1981) that anhydrite is a major hydrothermal mineral to be formed during the interaction of seawater with rhyolitic rocks at 200–500 °C. This is also supported by microbandings of oxidized hematite interlayered with mesobandings of anhydrite and halite as well as the presence of polygenetic glaciogenic dropstones in the salt minerals.

During the final stage of interglacial time, rapid melting of ice cover led to the marine transgression (Hoffman et al., 1998, 2011; Sankaran, 2003; Kennedy and Christie-Blick, 2011), sea-level rise, a change in water salinity, increasing water depth and deposition of cap carbonates. For comparison, Grotzinger and Al-Rawahi (2014) and Hebert et al. (2010) reported about six evaporite-carbonate cycles during the Late Ediacaran glaciation timeline in the Ara Group of Oman. The occurrence of the cap carbonates upon the banded iron-salt mineralization at the Hormuz Island may have followed the same geohistory. Houghton (1980) suggested that low bromide content of halite in the Hormuz Island is close to the meteoric water of a continental source. As such, it seems possible that the low bromide waters were formed by ice cove melting, followed by mixing with normal seawater. This indicates that the bromine content and salinity of the salts were decreased by huge volume of ice melted water, which led to transgression and deposition of the cap carbonates.

7.5.8. Stage 3: Deformation, folding and faulting

The Hormuz Complex includes synchronous felsic volcanic rocks and dropstone-bearing banded iron salt formation that were deposited syngenetically during the Ediacaran and were folded and faulted probably during the Late Pan-African orogen. Due to the lack of seismic and drilling data, it is not possible to present the exact structural and deformational geohistory of the Hormuz Complex. However, according to Fig. 3B and Fig. 12C, the steep dips (50–80 degree in Fig. 3B) are towards the peripheral parts of the Hormuz Island. Therefore, the overall concentric structure possibly resembles a dome–shaped anticlinorium, though Talbot et al. (2009) considered the whole structure to be a mushroom-shaped salt plug. The anticlinorium includes minor small faulted anticline, syncline and drag folds (Fig. 14A, B). Drag folds were probably formed as the incompetent banded hematite-salt rocks were subjected to shear deformation between the competent Precambrian basement rocks and the competent felsic rhyolitic domes. This seems likely as the banded iron salt formations were deposited among 25 felsic rhyolitic bodies (see Fig. 3B). Most of the faults occur as normal and low angle reverse faults, although Talbot et al. (2009) reported tear vertical faults in bedded salt rocks. The most significant point of the structural deformation is the absence of any metamorphic deformational texture in banded iron salt formation.

7.5.9. Stage 4: Supergene mineralization and karstification

Residual and supergene iron deposits are formed by hydration, oxidation, dissolution and leaching of soluble compounds due to circulation and downward percolation of groundwater on the precursor iron oxides, silicates and carbonates, followed by residual precipitation of secondary iron oxides, in particular red goethite-hematite. The process has been fully explained by Conliffe (2016) and Hagemann et al. (2016), where gangue minerals, hematite and goethite are dissolved, removed and deposited as red brown goethite and hematite. The best example of supergene banded iron formation is Minas Gerais in Brazil (Dorr, 1964), in which itabirites are disaggregated by partial dissolution of silica and are enriched in porous red brown goethite and hematite. In the Hormuz BISF the supergene dissolution, hydration and oxidation were the main controlling factors for the occurrence of earthy red brown ochre (Persian red) mine, secondary halite, gypsum and karstification features. Experimentally, the supergene decomposition of salts, silicate minerals, sulfides and carbonates and hydration of hematite produce red brown goethite at about less than 125 °C (Smith and Lidd, 1949). This is reflected in depletion of SiO_2, Na and Cl and residual enrichment of Fe_2O_3 as porous earthy red brown goethite and hematite. The residual supergene mineralization occurs as a thick red regolith, overlying the primary banded hematite-salt formation as well as inside the collapsed caves.

8. Conclusions

The most significant conclusions of this investigation are as the followings:

1. The U-Pb age data (558 ± 7 Ma) and the presence of genus Collenia in cap carbonates attest that the BISF at Hormuz Island is a new Ediacaran style of iron-salt mineralization, which is linked to synchronous alkaline A-type felsic volcanism.
2. The presence of well-defined macrobandings, mesobandings and microbanding in jaspilitic hematite-halite-anhydrite suggests the genetic model of banded iron salt formation.
3. The presence of of subrounded, rounded, bullet-shape, polygenic metamorphogenic dropstones in BISF documents the possible glaciogenic origin, which has not been recognized previously. This is also supported by the marked negative $\delta^{13}C$ excursion in cap carbonates, supporting the view of a new Late Ediacaran glaciation timeline (558 ± 7 Ma) in Iran.

4. The absence of compact breccia, flow structure and mylonitic texture in the dropstones-diamictites, indicates that the glaciogenic clasts may have not been emplaced or originated by fault scarps.

5. The REEs + Y data display LREE enrichment, strong Tb-Tm anomaly, a weak positive Y anomaly and no distinguished Eu or Ce anomaly. These are caused by the presence of dropstone inputs as well as dilution of hydrothermal fluids by seawater and ice melted water inputs.

6. The high values of Zr, Hf, Nb, Ta, Th, La, Ce and Y in BISF, dropstones, halite and cap carbonate are two magnitudes higher than the known BIFs worldwide. This is possibly related to the presence of detrital zircon, monazite and xenotime in glaciogenic dropstones.

7. The high ratios of Ni/Fe, P/Fe and the position of data on Fe/Ti versus Al/ Al + Fe + Mn + Ca + Na + K diagram correlate well with the exhalative hydrothermal Ediacaran-type banded iron salt formation.

8. The occurrence of actinolite, ripidolite, albite, epidote, sericite, tourmaline, clinochlore, anhydrite and clay minerals in altered proximal and distal zones reflects seawater-rhyolite interactions by circulating exhalative hydrothermal fluids. These mineral assemblages conform to the same minerals obtained by experimental seawater-felsic rock interactions at about 200–500 °C.

9. The frequent association of jaspilitic hematite, the absence of brecciated magnetite in the ore paragenesis and the low contents of Cu and gold in BISF do not support the IOCG or Kiruna–type model of iron mineralization.

10. This investigation highlights that A-type alkaline submarine felsic volcanism may be a new exploration target for Ediacaran banded iron salt formation.

Acknowledgements

References

Aftabi, A., 2001. Introduction to the iron ores of Bandar Abbas: a new model of Rapitan banded iron formation. J. Mines Metals 60–75, 53–66 (In Persian with English abstract).

Aftabi, A., Mohseni, S., Babaki, A., Azaraien, H., 2009. Fluid inclusion and stable isotope. study of the Esfordi apatite–magnetite deposit, central Iran – a discussion. Econ. Geol. 104, 137–139.

Aghanabati, A., 2004. Geology of Iran. Geological Survey of Iran, 619 p (In Persian).

Ahmadzadeh-Heravi, M., Houshmandzadeh, M., Nabavi, M.H., 1990. New concepts of Hormoz formation, s stratigraphy and the problem of salt diapirism in south Iran. Proc. Symp. Diapirism Special Reference to Iran 1, 1–21.

Ala, M.A., 1974. Salt diapirism in southern Iran. AAPG Bull. 58, 1758–1770.

Alavi, M., 2004. Regional stratigraphy of the Zagros fold-thrust belt of Iran and its proforeland evolution. Am. J. Sci. 304, 1–20.

Ali, K.A., Stern, R.J., Manton, W.I., Johnson, P.R., Mukherjee, S.K., 2010. Neoproterozoic diamictites in the eastern desert of Egypt and northern Saudi Arabia. Evidence of 750 Ma glaciations in the Arabian-Nubian Shield. Int. J. Earth Sci. (Geol. Rundsch) 99, 705–726.

Allan, J. R., Wiggins, W. D., 1993. Dolomite reservoirs: Geochemical techniques for evaluating origin and distribution. In: AAPG continuing educatio course notes36, American Association of Petroleum Geologists, 129p.

Atapour, H., Aftabi, A., 2012. Rapitan-type banded iron formation at Hormuz Island, Iran. Geological Survey of Iran. In: The 30th Geological Symposium, Programme with abstracts (In Persian with English abstract), 7p.

Atapour, H., Aftabi, A., 2017. Comments on "geochronology and geochemistry of rhyolites from Hormuz Island, southern Iran: A new Cadomian arc magmatism in the Hormuz Formation" by N. S. Faramarzi, S. Amini, A. K. Schmitt, J. Hassanzadeh, G. Borg, K. McKeegan, S. M. H. Razavi, S. M. Mortazavi, Lithos, Sep.

2015, 236–237, P.203-211. A missing link of Ediacaran A-type rhyolitic volcanism associated with glaciogenic banded iron salt formation (BISF): Lithos, DOI: 10.1016/j.lithos.2016.07.043.

Bacon, C.R., 2011. Magmatic Enclaves. American Geophysical Union.

Bekker, A., Palanavsky, N.J., Krapez, B., Rasmussen, B., Hofmann, A., Slack, J.F., Rouxel. O.J., Konhauser, K.O., 2014. Iron formations: Their origins and implications for ancient seawater chemistry: Treatise on Geochemistry, Second ed., 561–628p.

Baldwin, G.I., Turner, E.C., Kamber, B.C., 2012. A new depositional model for glaciogenic Neoproterozoic banded iron formation: Insights from the chemostratigraphy and basin configuration of the Rapitan banded iron formation. Can. J. Earth Sci. 49, 455–476.

Baldwin, G.I., 2014. The stratigraphy and Geochemistry of the Rapitan Formation, Northwest Territories and Yukon, Canada Unpublished Ph.D thesis. Laurentian University, Canada. 248 p.

Barnes, H.L., 1979. Geochemistry of Hydrothermal Ore Deposits. Wiley-Inerscience. 798 p.

Basta, F.F., Maurice, A.E., Fontbote, L., Favarger, P.Y., 2011. Petrology and geochemistry of the banded iron formation (BIF) of Wadi Karim and Um Anab, Eastern Desert, Egypt; Implications for the origin of Neoproterozoic BIF. Precambr. Res. 187, 277–292.

Bosak, P., Jaros, J., Spudil, J., Sulovsky, P., Vaclavek, V., 1998. Salt plugs in the eastern Zagros, Iran: Results of regional geological reconnaissance. Geolines 7, 172.

Burns, R.G., 1993. Rates and mechanism of chemical weathering of ferromagnesian silicate minerals on Mars. Geochim. Cosmochim. Acta 57, 4555–4674.

Clemens, J.D., Holloway, J.R., White, A.J.R., 1986. Origin of A-type granite: experimental constraints. Am. Mineral. 71, 317–324.

Conliffe, G., 2016. Geology and geochemistry of high-grade iron-ore deposits in the Kivivic Timmins and Ruth Lake areas, Western Labrador. Current Research, Newfoundland and Labrador Department of Natural Resources, Geological Survey, Report 16-1, p. 1–26.

Cox, K.G., Bell, J.D., Pankhurst, R.J., 1979. The Interpretation of Igneous Rocks. George Allen & Unwin, London, p. 450.

Cox, G.M., Halverson, G.M., Minarik, W.G., Le Heron, D.P.P., Acdonald, F.A., Bellefroid, E.J., Strauss, J.V., 2013. Neoproterozoic iron formation: an evaluation of its temporal, environmental and tectonic significance. Chem. Geol. 362, 232–249.

Daliran, F., 2002. Kiruna-type iron oxide-apatite ores and apatites of the Bafq district, Iran, with an emphasis on the REE geochemistry of their "apatites". In: Porter, T.M. (Ed.), Hydrothermal Iron Oxide Copper-Gold & related Deposits: A Global Perspective, vol. 2. PGC Publishing, Adelaide, pp. 303–320.

Deer, W.A., Howie, R.A., Zussman, J., 1977. An Introduction to the Rock Forming Minerals. Longman, Tenth Impression, p. 528.

Derry, L.A., Kaufman, A.J., Jacobsen, S.B., 1992. Sedimentary cycling and environmental change in the Late Proterozoic: evidence from stable and radiogenic isotopes. Geochim. Cosmochim. Acta 56, 1317–1329.

Dorr, J.V.N., 1964. Supergene ores of Minas Gerais, Brazil. Econ. Geol. 59, 1203–1240.

Eby, G.N., 1992. Chemical subdivision of the A-type granitoids. Petrogenic Tectonic Implications: Geol. 20, 641–644.

Eby, G.N., 2011. A-type granites: Magma sources and their contribution to the growth of the continental crust. In: Seven Hutton Symposium on granites and related rocks, p. 50–51.

Edgell, H.S., 1991. Proterozoic salt basins of the Persian Gulf area and their role in hydrocarbon generation. Precambr. Res. 54, 1–14.

El-Bialy, M.Z., Hassen, I.S., 2012. The Late Ediacaran (580–590 Ma) onset of anorogenic alkaline magmatism in the Arabian-Nubian shield: Katherina A-type rhyolites of Gabal Maain, Sinai. Egypt. Lithos. 216–219, 1–22.

Etemad-Saeed, N., Hosseini-Barzi, M., Adabi, M.H., Miller, N.R., Sadeghi, A., Houshmandzadeh, A., Stockli, D.F., 2015. Evidence for ca 560 Ma Ediacaran glaciation in the Kahar Formation, Central Alborz Mountains, northern Iran. Gondwana Res. 31, 164–183.

Faramarzi, N.S., Amini, S.M., Schmitt, A.K., Hassanzadeh, J., Borg, G., Mckeegan, K., Raszavi, S.M.H., Mortazavi, S.M., 2015. Geochronology and geochemistry of rhyolites from Hormuz Island, southern Iran. A new record of Cadomian arc magmatism in the Hormuz Formation. Lithos. 236–237, 203–211.

Fike, D.A., Grotzinger, J.P., Pratt, I.M., Summons, R.E., 2006. Oxidation of Ediacaran ocean. Nature 444, 744–747.

Fike, D.A., Grotzinger, J.P., 2008. A paired sulfate-pyrite 34 S approach to understanding the evolution of the Ediacaran –Cambrian sulfur cycle. Geochim. Cosmochim. Acta 72, 2636–2648.

Font, E., Nedelec, A., Trindade, R.I.F., Macouin, M., Charriere, A., 2006. Chemostratigraphy of the Neoproterozoic Mirasoll d, Oeste cap dolostones (Mato Grosso), Brazil. An alternative model for Marionoan cap dolostone formation. Earth Planet. Sci. Lett. 250, 89–103.

Force, E.R., Eidel, J.J., Maynard, J.B., 1991. Sedimentaty and diagenetic mineral deposits: a basin analysis approach to exploration. Rev. Econ. Geol. 5, 143–144.

Forster, H., Jafarzadeh, A., 1994. The Bafq mining district in central Iran-a highly mineralized Infracamb rian volcanic field. Econ. Geol. 89, 1697–1721.

Gansser, A., 1992. The enigma of the Persian salt dome inclusions: Eclogae Geol. Helv. 85, 825–846.

Gaucher, C., Sial, A.N., Frei, R., 2015. Chemostratigraphy of Neoproterozoic banded iron formation (BIF). Types, Age and Origin, Chemostratigraphy. Elsevier, pp. 433–445. Chapter 17.

Ghazban, F., 2009. Petroleum Geology of the Persian Gulf. University of Tehran Press. 707p.

Ghazban, F., Al-Aasm, I.S., 2010. Hydrocarbon–induced diagenetic dolomite and pyrite formation associated with the Hormuz Island salt dome, offshore Iran. J. Pet. Geol. 32, 1–14.

Goudie, A.S., 2004. Encyclopedia of Geomorphology. Taylor & Francis Group. 1202p.

Grotzinger, J., Al-Rawahi, Z., 2014. Depositional facies and platform architecture of microbialite-dominated carbonate reservoirs, Ediacaran-Cambrian Ara Group, Sultanate of Oman. Am. Assoc. Pet. Geol. 98, 1453–1494.

Hagemann, S.G., Angerer, T., Duuring, P., Rosiere, C.A., Figueiredo e Silva, R.C., Lobato, L., Hensler, A.S., Walde, D.H.G., 2016. BIF-hosted iron mineral system. Rev. Ore Geol. Rev. 76, 317–359.

Hajash, A., Chandler, G.W., 1981. An experimental investigation of high-temperature interactions between seawater and rhyolite, andesite, basalt and peridotite. Contrib. Mineralog Petrol. 78, 240–254.

Halverson, G.P., Wade, B.P., Hurtgen, M.T., Barovich, K.M., 2010. Neoproterozoic chemostratigraphy. Precambr. Res. 182, 337–350.

Hebert, C.L., Kaufman, A.J., Penniston-Dorland, S.C., Martin, A.J., 2010. Radiometric stratigraphic constraints on terminal Ediacaran (post-Gaskiers) glaciation and metazoan evolution. Precambr. Res. 182, 402–412.

Heidarian, H., Alirezaei, S., Lentz, D.R., 2017. Chadormalu Kiruna-type magnetite-apatite, Bafq district, Iran: Insights from hydrothermal alteration and petrogenesis from geochemical, fluid inclusion, and sulfur isotope data. Ore Geol. Rev. 83, 43–62.

Hoffman, P.F., Kaufman, A.J., Halverson, G.P., Schrag, D.P., 1998. A Neoproterozoic Snowball Earth. Science 281, 1342–1346.

Hoffman, P.F., Macdonald, F.A., Halverson, G.P., 2011. Chemical sediments associated with Neoproterozoic glaciation: iron formation, cap carbonates, barite and phosphorite. Geol. Soc. London, Memoir 36, 67–80.

Holland, H.D., 2005. Sedimentary mineral deposits and the evolution of earth nearsurface environments. Econ. Geol. 100, 1489–1509.

Horton, B.K., Hassanzadeh, J., Stockli, D.F., Axen, G.J., Gillis, R.G., Guest, B., Amini, S., Fakhari, M.D., Zemanzadeh, S.M., Grove, M., 2008. Detrital zircon provenance of Neoperoterozoic to Cenozoic deposits in Iran: Implications for chronostratigraphy and collisional tectonics. Tectonophysics 451, 97–122.

Houghton, M.L., 1980. Geochemistry of the Proterozoic Hormuz Evaporates, Southern Iran. M.Sc. thesis.

Hovland, M., Rueslatten, H.G., Johnsen, H.K., Kvamme, B., Kuzenetsova, T., 2006. Salt formation associated with sub-surface boiling and supercritical water. Mar. Pet. Geol. 23, 855–869.

Hurford, A.J., Grunau, H.R., Stocklin, J., 1984. Fission track dating of an apatite crystal from Hormuz Island, Iran. J. Pet. Geol. 7, 365–380.

Houshmandzadeh, A., Hamdi, B., Nabavi, M.H., 1988. Precambrian-Lower Cambrian strata in Iran. In: Proceeding of Symposium in mineral resources of Yazd province. Ministry of Mines and Metals, p. 372–469 (In Persian).

Husseini, M.I., 1988. The Arabian Infracambrian extensional system. Tectonophysics 148, 93–103.

Ilyin, A.V., 2009. Neoproterozoic banded iron formations. Lithol. Min. Resour. 44, 78–85.

Jafarzadeh, A., Ghorbani, M., Pezeshkpour, M., 1996. Geology of Iran. Iron deposits: Ministry of Mines and Metals, no. 26, 214 p.

Kavana, E., 2015. Geological mapping, structural setting and petrographic description of the Archean volcanic rocks of Mnanka area, North Mara, Tanzania. In: Proceedings World Geothermal Congress, Melbourne, Australia, 19–25 April, 1–16.

Kennedy, M.J., Christie-Blick, N., 2011. Condensation origin for Neoproterozoic cap carbonates during deglaciation. Geology 39, 319–322.

Kent, P.E., 1979. The emergent of salt plugs of southern Iran. J. Pet. Geol. 2, 117–144.

Kimura, H., Matsumoto, R., Kakuwa, Y., Hamdi, B., Zibaseresht, H., 1997. The Vendian-Cambrian $\delta^{13}C$ record, North Iran: Evidence for overturning of the ocean before the Cambrian explosion. Earth Planet. Sci. Lett. 147, E1–E7.

Klein, C., Beukes, D.J., 1993. Sedimentology and geochemistry of the glaciogenic Late Proterozoic Rapitan iron formations. Econ. Geol. 88, 542–565.

Krauskopf, K.B., 1967. Introduction to Geochemistry. MC Graw-Hill. 721 p.

Kroner, A., Stern, R.J., 2005. Pan-African Orogeny. Encyclopedia of Geology, vol. 1. Elsevier, pp. 1–12.

Le Heron, D.P., Tofaif, S., Vandyk, T., Ali, D.O., 2017. A diamictite dichotomy: Glacial conveyor belts and olistostromes in the Neoproterozoic of Death Valley, California, USA. Geology 45, 31–34.

Lottermoser, B.G., Ahshley, P.M., 2000. Geochemistry, petrology and origin of Neoproterozoic ironstones in the eastern part of the Adelaide geosynclines, south Australia. Precambr. Res. 101, 49–67.

Loyd, S.J., Crsetti, F.A., Eagle, R.A., Hagadorn, Y., Shen, X., Bonifacie, M., Tripati, A.K., 2015. Evolution of Neoproterozoic Wonoka-Shuram anomaly-aged carbonates. Evidence from clumped isotope paleothermometry. Precambrian Res. 264, 179–191.

Marzouk, I., El-Sattar, M. A., 1994. Wrench tectonics in Abu Dhabi, United Arab Emiarates, In M. I. Al-Husseini, ed., Middle East Petroleum Geocsciencwees, GEO, 94. Gulf Petrolink 1, pp. 655-668

Mason, B., Moore, C.B., 1982. Principles of Geochemistry. John Wiley & Sons, p. 344.

McClellan, E., Gazel, E., 2014. The Cryogenian intra continental rifting of Rodinia: Evidence from the Laurentian margin in eastern North America. Lithos 206–207, 321–337.

Mohseni, S., Aftabi, A., 2015. Structural, textural, geochemical and isotopic signatures of synglaciogenic Neoproterozoic banded iron formations (BIFs) at Bafq mining district (BMD, Central Iran. The possible Ediacaran missing link of BIFs in Tethyan metallogeny. Ore Geol. Rev. 71, 215–236.

Momenzadeh, M., 2007. Saline deposit and alkaline magmatism; a genetic model. J. Pet. Geol. 13, 341–356.

Nasir, S., Al-Saad, H., Alsayigh, A., Weidlich, O., 2008. Geology and petrology of the Hormuz dolomite, Infracambrian: implications for the formation of the salt-cored Halul and Shraouh Islands, offshore, state of Qatar. J. Asian Earth Sci. 33, 353–365.

Padyar, F., Borna, B., Ghorbani, M., Alizadeh, V., Jafarzadeh, N., 2012. Fluid inclusions and raman spectroscopic study in apatite of Hormuz Island. Geological Survey of Iran. In: The 30th Geological Symposium, Programme with abstracts (In Persian with English abstract) 9 p.

Pearce, J.A., Harris, N.B.W., Tindle, A.G., 1984. Trace element discrimination diagrams for the tectonic interpretation of granitic rocks. J. Petrol. 25, 956–983.

Pecoits, E., Gingras, M.K., Barley, M.E., Kappler, A., Posth, N.R., Konhauser, K.O., 2009. Petrography and geochemistry of the Dales Gorge banded iron formation: paragenetic sequence, source and implications for paleo-ocean chemistry. Precambr. Res. 172, 163–187.

Pelleter, E., Cheillez, A., Gasquet, D., Mottaqi, A., Annich, M., El Hakour, A., 2006. Discovery of Neoproterozoic banded iron formation(BIF) in Morocco. Eur. Geosci. Union. Geophys. Res. Abstr. 8, 3.

Pettijohn, F.J., 1975. Sedimentary Rocks. Harper & Row, p. 628.

Pirajno, F., 2009. Hydrothermal Processes and Mineral Systems. Springer, p. 1250.

Player, R.A., 1969. The Hormuz Salt Plugs of Southern Iran. University of Reading, Reading England. Unpublished Ph.D thesis.

Ramazani, J., Tucker, R.D., 2003. The Saghand region, Central Iran: U-Pb geochronology, petrogenesis and implications for Gondwana tectonics. Am. J. Sci. 303, 622–665.

Sagiroglu, A., Kara, H., Kurum, S., 2013. Hematite muscovite schists of Malatya, Turkey: could it be the first known banded iron formation (BIF) in the Taurids and Anatolia? Carpathian J. Earth Environ. Sci. 8, 1–2.

Sankaran, A.V., 2003. Neoproterozoic snowball earth and the cap carbonates. Curr. Sci. 84, 871–873.

Self, S., 2006. The effects and consequences of very large explosive volcanic eruptions. Philos. Trans. R. Soc. 364, 2073–2097.

Seyfried, W.E., Bischoff, J.L., 1977. Hydrothermal transport of heavy metals by seawater, The role of seawater/basalt ratio. Earth Planet. Sci. Lett. 34, 71–77.

Shields, G.A., 2005. Neoproterozoic cap carbonates: a critical appraisal of existing models and the plumeworld hypothesis. Terra Nova 17, 299–310.

Slack, J.F., 1993. Models for tourmalinite formation in the Middle Proterozoic Belt and Purcell supergroups (Rocky Mountain) and their exploration significance. Geological Survey of Canada, Current Research Paper93-1E, 33–40.

Slack, J.F., Trumbull, 2011. Tourmaline as a recorder of ore-forming processes. Elements 7, 321–326.

Smith, F.G., Lidd, D.J., 1949. Hematite-goethite relations in neutral and alkaline solutions under pressure. Am. Mineral. 34, 403–412.

Smith, A.G., 2012. A review of the Ediacaran to Early Cambrian (Infracambrian) evaporites and associated sediments of the Middle East. Geol. Soc., London, Special Publ. 366, 229–250.

Stern, R.J., Avigad, D., Miller, N.R., Beyth, M., 2006. Evidence for the snowball Earth hypothesis in the Arabian-Nubian shield and the east Africal Orogen. J. Afr. Earth Sci. 44, 1–20.

Stern, R.J., Avigad, D., Miller, N., Beyth, M., 2008. From volcanic winter to Snowball Earth: an alternative explanation for Neoproterozoic biosphere stress. In: Dilek, Y. et al. (Eds.), Links Between Geological Processes, Microbial activities and Evolution of Life. Springer, pp. 313–336.

Stewart, F.H., 1963. Data of geochemistry, Chapter Y, marine evaporates. Geological Survey of America, Professional Paper 440-Y.

Stocklin, J., 1968. Structural history and tectonics of Iran. Rev.: Bull. Am. Assoc. Pet. Geol. 52, 1229–1258.

Stocklin, J., Setudehnia, A., 1991. Stratigraphic lexicon of Iran. Geological Survey of Iran, Report 18, 376 p.

Sun, S.S., McDonough, W.F., 1989. Chemical and isotopic systematics of ocean basalts: Implications for mantle composition and processes. In: Saunders, A.D., Nory, M.J. (Eds.), Magmatism in Oceanic Basin, vol. 42. Geological Survey of London, Special Publication, pp. 313–345.

Strauss, H., 1993. The sulfur isotopic record of Precambrian sulfates. New data and a critical evaluation of the existing record. Precambr. Res. 63, 225–246.

Syme, E.C., 1998. Ore associated and barren rhyolites in the central Flin Flon Belt. Case study of the Flin Flon mines sequence: Manitoba Energy and Mine, open File Report 98-9, pp. 1–17.

Talbot, C., Aftabi, P., Chemia, Z., 2009. Potash in a salt mushroom at Hormuz Island, Hormuz Strait, Iran. Ore Geol. Rev. 35, 317–332.

Thompson, A.J.B., Thompson, J.F.H., 1996. Atlas of Alteration. A field and petrographic guide to hydrothermal alteration minerals. Geological Association of Canada, Mineral Deposits Division, p. 128.

Tivey, M.K., 2007. Generation of seafloor hydrothermal vent fluids and associated mineral deposits. Oceanography, 312.

Tucker, M.E., 1991. Sedimentary Petrology. Blackwell. 260 p.

Vernhet, E., Youbi, N., Chellai, E.H., Villeneuve, M., Archi, A., 2012. The Bou-Azzer glaciation: Evidence for an Ediacaran glaciation on the West African Craton (Anti-Atlas, Morocco). Precambr. Res. 196–197, 106–112.

Waitt, R.B., 2013. Lahar. In: Bobrowsky, P.T. (Ed.), Encycopedia of Natural Hazards. Springer.

Walther, H.W., 1968. The genesis of iron ore of the Hormuz Series near Bandar Abbas. In: 23rd International Geological Congress, Prague, part 7.

Warren, J.K., 2006. Evaporites, Sediments, Resources and Hydrocarbons. Springer, Berlin, p. 1036.

Warren, J.K., 2012. Evaporites through time: tectonic, climate and eustatic controls in marine and nonmarine deposits. Earth Sci. Rev. 98, 217–268.

Wen, B., Evans, D.A.D., Li, Y.X., Wang, Z., Liu, C., 2015. Newly discovered Neoproterozoic diamictite and cap carbonate (DCC) couplet in Tarim craton, NW China: Stratigraphy, geochemistry, and paleoenvironment. Precabmrian Res. 271, 278–294.

Williams, P.J., Barton, M.D., Johnson, D.A., Fontbote, L., De Haller, A., Mark, G., Oliver, N.H.S., Marschik, R., 2005. Iron oxide copper-gold deposits: Geology, space-time distribution, and possible mode of origin. In: Economic Geology, 100th Anniversary volume, p. 371–405.

Winchester, J.A., Floyd, P.A., 1977. Geochemical discrimination of different magma series and their differentiation products, using immobile elements. Chem. Geol. 20, 325–343.

Yeo, G.M., 1981. In: Campbell, F.H.A. (Ed.), Geological Survey of Canada, pp. 25–46. Paper 81.

Young, G.M., 2002. Stratigraphic and tectonic setting of Proterozoic glaciogenic rocks. J. African Earth Sci. 35, 451–466.

Young, G.M., 2013. Evolution of earth, climatic system. Evidence from ice ages, isotopes and impacts. GSA Today 23, 4–10.